

Panchromatic Properties of the Extreme Fe II Emitter PHL 1092

Murilo Marinello^{1*}, Alberto Rodríguez-Ardila^{1,2}, Paola Marziani³, Aaron Sigut⁴,
Anil Pradhan⁵

¹Laboratório Nacional de Astrofísica – Rua dos Estados Unidos 154, Bairro das Nações. CEP 37504-364, Itajubá, MG, Brazil

²Divisão de Astrofísica - INPE, Avenida dos Astronautas 1758, 12227-010, S.J.Campos-SP, Brazil

³INAF, Osservatorio Astronomico di Padova, vicolo dell Osservatorio 5, IT 35122, Padova, Italy

⁴Department of Physics and Astronomy, The University of Western Ontario, London, Ontario N6A 3K7, Canada

⁵McPherson Laboratory, The Ohio State University, 140 W. 18th Ave., Columbus, OH 43210-1173, USA

Accepted XXX. Received YYY; in original form ZZZ

ABSTRACT

We present near-infrared spectroscopy of the NLS1 galaxy PHL 1092 ($z = 0.394$), the strongest Fe II emitter ever reported, combined with optical and UV data. We modeled the continuum and the broad emission lines using a power-law plus a black body function and Lorentzian functions, respectively. The strength of the Fe II emission was estimated using the latest Fe II templates in the literature. We re-estimate the ratio between the Fe II complex centered at 4570 Å and the broad component of H β , R_{4570} , obtaining a value of 2.58, nearly half of that previously reported ($R_{4570}=6.2$), but still placing PHL 1092 among extreme Fe II emitters. The FWHM found for low ionization lines are very similar ($\text{FWHM}\sim 1200 \text{ km s}^{-1}$), but significantly narrower than those of the Hydrogen lines ($\text{FWHM}_{\text{H}\beta} \sim 1900 \text{ km s}^{-1}$). Our results suggest that the Fe II emission in PHL 1092 follows the same trend as in normal Fe II emitters, with Fe II being formed in the outer portion of the BLR and co-spatial with Ca II, and O I, while H β is formed closer to the central source. The flux ratio between the UV lines suggest high densities, $\log(n_{\text{H}})\sim 13.0 \text{ cm}^{-3}$, and a low ionization parameter, $\log(U)\sim -3.5$. The flux excess found in the Fe II bump at 9200 Å after the subtraction of the NIR Fe II template and its comparison with optical Fe II emission suggests that the above physical conditions optimize the efficiency of the Ly α -fluorescence process, which was found to be the main excitation mechanism in the Fe II production. We discuss the role of PHL 1092 in the Eigenvector 1 context.

Key words: galaxies: active – techniques: spectroscopic – individual: PHL 1092

1 INTRODUCTION

Narrow-line Seyfert 1 (NLS1) galaxies are a particular subclass of active galactic nuclei (AGN) that show narrow permitted emission lines ($\text{FWHM}_{\text{H}\beta} < 2000 \text{ km/s}$) and weak [O III] $\lambda\lambda 4959, 5007$ lines ($[\text{O III}]/\text{H}\beta < 3$) (Osterbrock & Pogge 1985; Goodrich 1989) than classical Type I AGN. Besides, NLS1 have other interesting properties across the electromagnetic spectrum. In the optical and UV they show strong asymmetries in the [O III] lines (Zamanov et al. 2002; Bian et al. 2005; Boroson 2005) and high velocity blueshifted C IV lines (Sulentic et al. 2000c, 2002; Wills et al. 2000; Leighly & Moore 2004). One of the most intriguing prop-

erties of NLS1 is the strong Fe II emission, with numerous multiplets across the UV, optical and NIR spectrum that form a pseudo-continuum mostly in the UV and optical regions. The strength of this feature, usually represented by the flux ratio Fe II/H β between the Fe II bump centred at 4570 Å and the broad component of H β (hereafter R_{4570}), is about twice or larger than that measured in normal AGN (Zhou et al. 2006), with NLS1 reaching values higher than 1 (Joly 1991; Marziani et al. 2001; Shen et al. 2011; Rakshit et al. 2017).

Several models have tried to explain the Fe II emission in AGN. The most recent ones incorporate excitation mechanisms such as collisional excitation, continuum fluorescence, self-fluorescence of Fe II lines and Ly α -fluorescence (Sigut & Pradhan 1998; Verner et al. 1999; Sigut & Pradhan

* E-mail: murilo.marinello@gmail.com

2003; Bruhweiler & Verner 2008; Pradhan & Nahar 2011). A decade ago, Bruhweiler & Verner (2008) considerably improved this approach by considering an Fe II ion with 830 levels, noticing that an appropriate number of energy levels must be taken into account in order to reproduce the observed Fe II emission. Understanding this emission in AGN is important at least for 4 reasons: (i) the Fe II emission is one of the strongest cooling agents in the broad line region (BLR). It accounts for up to 25% of the total energy output of that emission region (Wills et al. 1985); (ii) it represents a strong component all over the spectrum. The myriads of Fe II multiplets forms a pseudo-continuum from the UV to NIR (Sigut & Pradhan 2003) with more than 344,000 transitions (Bruhweiler & Verner 2008). (iii) The gas emitting Fe II probes the structure and kinematics of the BLR (Kovačević et al. 2010; Hu et al. 1998; Sameshima et al. 2011; Martínez-Aldama et al. 2015; Cracco et al. 2016). (iv) The strength of Fe II relative to the peak of [O III] and width of the H β line forms the optical plane of the Eigenvector 1 (hereafter E1) (Boroson & Green 1992). It is believed to be associated to fundamental properties of AGN such as the accretion power and super massive black hole mass (Boroson & Green 1992; Sulentic et al. 2000c; Shen & Ho 2014).

Boroson & Green (1992) studied correlations among observed features in a complete radio-quiet sample of quasars using the Principal component analysis (PCA) technique. They found that most of the quasar properties are related to Eigenvector 1. E1 was later expanded to a 4-dimension eigenvector 1 (4DE1) parameter system to include the blueshift of C IV and the X-ray photon index (Sulentic et al. 2000c, 2002, 2007). The 4DE1 defines a main sequence for quasars that is believed to be ultimately driven by the Eddington ratio (L/LEdd) (Marziani et al. 2001; Shen & Ho 2014) and that, in addition to the four parameters of 4DE1, is correlated with low- and high-ionisation line profiles, systematic shifts of broad and narrow high-ionization lines (see Marziani et al. 2018, for a review). Moreover, it is possible to identify two populations of type-I AGN in the optical plane of the 4DE1 (defined by the FWHM(H β) and the R₄₅₇₀): “Population A” AGN, with FWHM(H β) < 4000 km s⁻¹ and strong Fe II emission; and “Population B” AGN, characterized by FWHM(H β) > 4000 km s⁻¹ and weaker Fe II emission (Sulentic et al. 2000a,b, 2002). More recently, Panda et al. (2018) showed that the Eddington ratio is not enough to drive the quasars through the E1 sequence, suggesting that higher abundances and high densities may also be necessary to place AGN at the high R₄₅₇₀ end of the E1. Marziani et al. (2001), while looking for a physical interpretation of the E1, pointed out to one particular AGN –PHL 1092– as an extreme outlier in the high-end of strong Fe II emitters. They considered this source as a rare case that should probe extreme conditions in the BLR.

PHL 1092 is a relatively nearby radio-quiet quasar ($z = 0.396$) with many interesting properties all over the electromagnetic spectrum. Its X-ray emission is known as one of the weakest and variable in a non-BAL AGN spectrum (Miniutti et al. 2009). In the UV, broad C IV and Ly α lines, with a high blueshifted and asymmetric profile in C IV are observed (Miniutti et al. 2012). The Near-UV spectrum is dominated by the pseudo-continuum formed by Fe II. In the optical region its outstanding Fe II emission reaches extreme values, with R₄₅₇₀ varying from 1.81 to 6.2 (Lawrence et al. 1997;

Bergeron & Kunth 1980). The main cause of this extreme variation is attributed to the method employed in measuring the optical Fe II emission. The narrowness of the Balmer lines (FWHM \sim 1800km/s) and the low ratio [O III]/H β \sim 0.9, together with the strong Fe II emission, classify this AGN as a high luminosity NLS1 (Osterbrock & Pogge 1985). Although PHL 1092 was already observed in many regions of the electromagnetic spectrum, to the best of our knowledge, no report of its properties in the NIR exists up to today.

The NIR has several advantages over the UV and optical for the study of the Fe II emission. For instance, the most conspicuous Fe II lines are nearly isolated features, allowing an accurate analysis of their intensities and line profiles. Moreover, emission lines, such O I and Ca II are isolated or moderately blended with adjacent lines (Martínez-Aldama et al. 2015; Marinello et al. 2016). While in the optical H β is severely affected by the underlying Fe II, the Paschen lines in the NIR are completely isolated (Rodríguez-Ardila et al. 2002). As pointed out by Sigut & Pradhan (1998, 2003); Rodríguez-Ardila et al. (2002) and (Marinello et al. 2016), this spectral window holds key features for understanding the physics of Fe II in AGN. For example, the Fe II bump centered at λ 9200 and the four isolated Fe II lines at λ 9998, 10502, 10900, 11127 Å (known collectively as the 1 μ m Fe II lines), carry important information about the excitation mechanisms of this ion (Sigut & Pradhan 1998, 2003; Marinello et al. 2016). Therefore optical and NIR observations combined improves the description of the excitation mechanism behind the extreme Fe II emission in this source.

In this paper we analyze for the first time NIR spectroscopy of PHL 1092 in combination with optical observations around the H β region in order to obtain a full coverage of the most important Fe II features of this source. Our goals are threefold: (i) To obtain a consistent estimation of the Fe II intensity; (ii) to measure the Fe II and other BLR features (H I, O I and Ca II) in order to get clues about the location, excitation mechanism, and physical conditions of the regions where they are emitted; (iii) To study the role of the PHL 1092 in the E1 context.

This paper is structured as follow: Section 2 presents the observations and data reduction. Section 3 describes the technique applied to fit the Fe II templates and measuring the emission lines properties of the broad lines in the observed spectra. Section 3 and 4 discusses the location of the Fe II emitting region, its physical conditions and the excitation mechanism driving this emission. The role of PHL 1092 in the E1 context is presented in Section 5. Conclusion are given in section 6.

2 OBSERVATIONS

2.1 GNIRS/Gemini spectroscopy

NIR spectra of PHL 1092 were obtained during the night of August 17, 2014, with the 8.1 m Gemini North telescope in Mauna Kea Observatory (Program ID GN-2014B-Q-29). We employed the Gemini Near-IR spectrograph (GNIRS, Elias et al. 2006) in the cross-dispersed mode, which allows simultaneous z+J, H and K band observations, covering the spectral range 0.8 – 2.5 μ m in a single exposure. The average seeing of the night was 0.7 arcsecs. The instrument setup

includes a 32 l/mm grating and a 0.8×15 arcsec slit, giving a spectral resolution of $R \sim 1300$. Individual exposures of 180 s each were taken, nodding the source in a pattern ABBA along the slit, with a total integration time of 36 minutes. Right after the observation of the science frames, an A0V star was observed at a similar airmass, with the purpose of flux calibration and telluric correction.

The NIR data were reduced using the XDNIRS pipeline (v2.0)¹, which delivers a full reduced, wavelength and flux calibrated, 1D spectrum with all orders combined (see Mason et al. 2015, for a more detailed description of the software). Briefly, the pipeline cleans the 2D images from radiative events and prepares a master flat constructed from quartz IR lamps to remove pixel to pixel variation. Thereafter, The s-distortion solution is obtained from daytime pinholes flats and applied to the science and telluric images to rectify them. Arc images are used to find the wavelength dispersion solution. The 1D spectrum is then extracted from the combined individual exposures. The telluric features from the science spectrum are removed using the spectrum of a A0V standard star. Finally, the flux calibration was achieved assuming a black body shape for the standard star (Pecaut & Mamajek 2013) scaled to its K-band magnitude (Skrutskie et al. 2006). The orders are finally combined in to a single spectrum as shown in the top panel of Figure 1.

2.2 Goodman/SOAR spectroscopy

Optical spectroscopy of PHL1092 was obtained on the night of December 12, 2014, with the 4.1 m Southern Observatory for Astrophysical Research (SOAR) Telescope at Cerro Pachon, Chile. The observations were carried out using the Goodman Spectrograph (Clemens et al. 2004), equipped with a 400 l/mm grating and a 0.8 arcsec slit width, giving a resolution $R \sim 1500$. The target was observed for a total of 45 minutes in three individual exposures of 15 minutes each. The standard star LTT 1020 was observed for flux calibration. HgAr arc lamps were observed after the science frames for wavelength calibration. Daytime calibrations include bias and flat field images.

The optical data was reduced using standard IRAF tasks. First, the bias frames were combined and subtracted from the remaining images. The images were then divided by a single averaged and normalized master flatfield image. The wavelength calibration of the science and star frames were achieved by applying the dispersion solution obtained from the arc lamp frames. The 1D spectra of LTT 1020 were then extracted and combined to derive the sensitivity function, later applied to the PHL 1092 1D spectrum. The two atmospheric bands, at 6870 and 7600 Å, were modeled and removed using the following procedure. First, we interpolate the continuum between the two ends of each atmospheric bands. Second, we divided the original standard star spectrum to that without the atmospheric bands. The ratio between them produce a template were the continuum is equal to one except in the regions containing the atmospheric bands. Third, We divided the PHL 1092 spectrum to that of the template. The final flux calibrated optical

spectrum of PHL 1092 is shown in the middle panel of the Figure 1.

2.3 STIS/HST spectroscopy

Ultraviolet spectroscopy for PHL 1092 was available at the Hubble Space Telescope science archive. The spectrum was taken on August 20, 2003 using the Space Telescope imaging Spectrograph (STIS) in combination with the filter G230L and a total integration time of 5746 s. It covers the rest frame wavelength interval 1120 Å – 2240 Å with a resolution of $R \sim 600 \text{ km s}^{-1}$. The bottom panel of the Figure 1 shows the UV HST spectrum with the emission lines relevant to this work identified by black arrows.

Note that neither UV, optical nor NIR spectra of PHL 1092 were taken simultaneously. As no overlap region exists between the different data sets, no effort was made to put them into a common flux level mostly because of potential variability effects, which may produce relative shifts between the continuum levels and emission lines along the UV, optical and infrared regions. However, the spectral gap between the optical and NIR observations is only 300 and the continuum flux at the red end of the Goodman spectrum and blue edge of the GNIRS spectrum is consistent with an underlying power-law continuum (see figure 1). This consistency suggest no (or very small) variability between the two observations. Assuming a conservative scenario, we consider the mean value of AGN fractional variability from Kollatschny et al. (2006) as representative of the variability effect in PHL 1092. They estimated an uncertainty of $\sim 11\%$ on the optical fluxes due to variability. Du et al. (2018) found a fractional variability $\lesssim 10\%$ for a sample of high accretion rate AGN. This value is also in good agreement with Hu et al. (2015), who found an average fractional variability of 10% for Fe II when compared with H β . Therefore, we use this values as a variability bias on all our measurements in this work.

3 SPECTRAL FEATURES

3.1 Continuum and Fe II Emission

In order to measure the Fe II content in PHL 1092 we first carry out a proper continuum emission subtraction. To this purpose, we assume that the rest-frame UV to optical continuum is represented by a power-law function. Besides, hundreds of thousands of blended Fe II multiplets form a pseudo-continuum from UV to NIR (Sigut & Pradhan 2003). Because both components are spatially unresolved, it is not possible to measure them independently. Moreover, in moderate to strong Fe II emitters, it is difficult to find out spectral windows free of both continua. Therefore, in order to disentangle them, the best approach is to model these two components simultaneously.

The Fe II emission is best represented by templates, usually derived from I Zw 1, the prototype NLS1. In the optical, Boroson & Green (1992) constructed an empirical template of the Fe II from the I Zw 1 spectrum by removing all other lines different from Fe II in that AGN. Vestergaard & Wilkes (2001) employed a similar approach to obtain an empirical

¹ Based on the Gemini IRAF packages

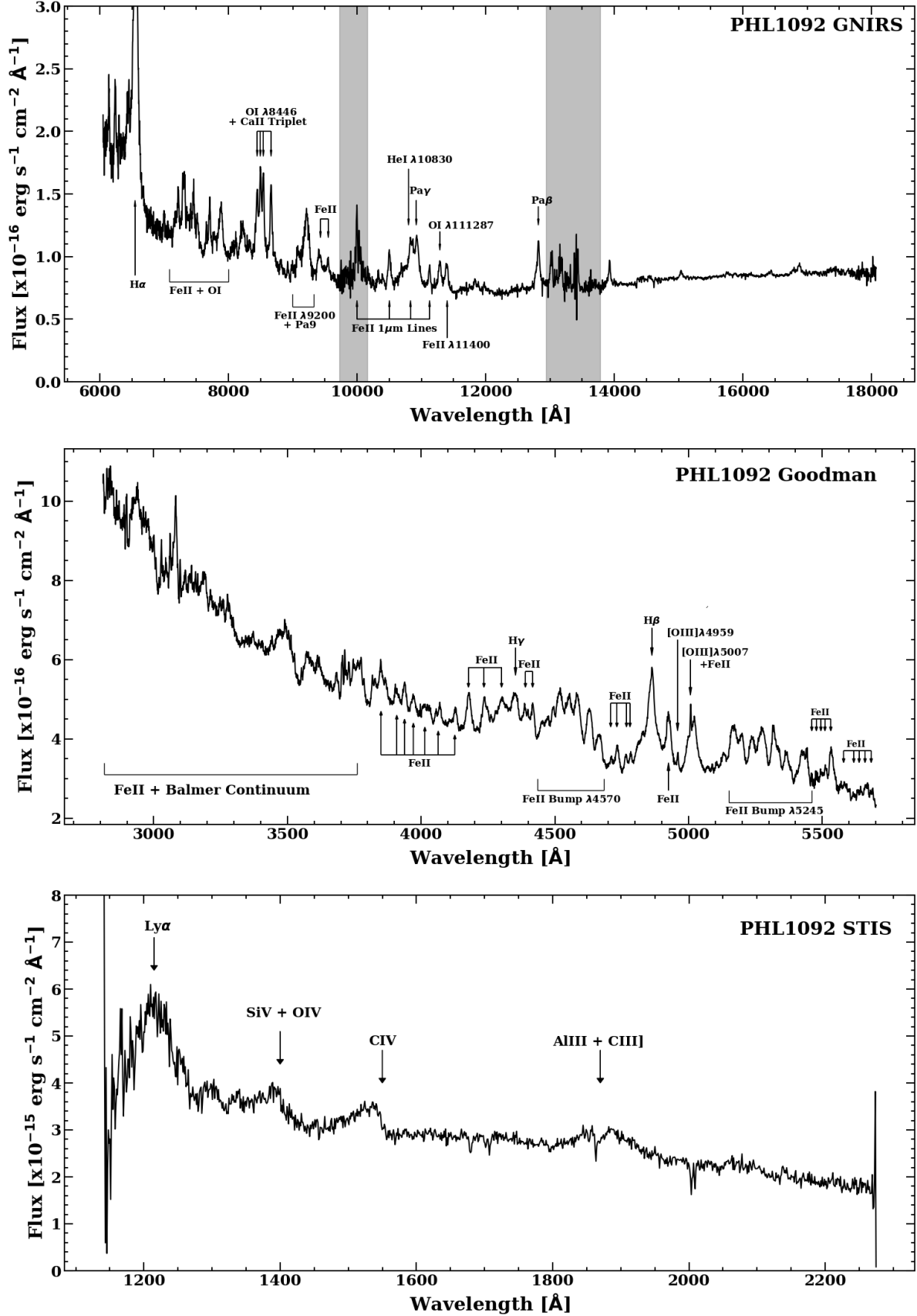


Figure 1. Observed PHL 1092 spectrum with GNIRS, Goodman, and STIS. The spectra were corrected by redshift, $z = 0.396$. Top panel: Full reduced and flux calibrated NIR spectrum of PHL 1092 observed with GNIRS/Gemini North. The gray shade areas mark the regions affected by telluric absorption. Middle panel: Fully reduced and flux calibrated optical spectrum of PHL 1092 observed with Goodman/SOAR. Bottom panel: Ultraviolet spectrum of PHL 1092 as observed by STIS/HST. In all three panels, prominent emission lines and Fe II multiplets are identified by the arrows.

UV template of this ion using a high S/N spectrum of I Zw 1 observed with HST/STIS.

Other authors have constructed templates using theoretical models based on assumptions about the physical conditions in the Fe II emission region. [Kovačević et al. \(2010\)](#), for instance, used the relative intensities of groups of multiplets and physical constraints to construct their template. [Tsuzuki et al. \(2006\)](#) combined the empirical approach of [Boroson & Green \(1992\)](#) and [Vestergaard & Wilkes \(2001\)](#) with theoretical models of the Fe II lines using CLOUDY ([Ferland et al. 1999](#)) to develop their templates. In the NIR, the only template available in the literature is from [Garcia-Rissmann et al. \(2012\)](#). It covers the wavelength interval 8000–11600 Å and was constructed using a semi-empirical approach, that is, by combining [Sigut & Pradhan \(2003\)](#) models with modifications to match the observed spectrum of I Zw 1. [Marinello et al. \(2016\)](#) and [Martínez-Aldama et al. \(2015\)](#) already demonstrated that this template successfully reproduces the NIR Fe II emission in several AGN.

Thus, in order to fit the optical continuum of PHL 1092 we will use a power-law plus the Fe II template from [Boroson & Green \(1992\)](#). Because the lines of our interest are concentrated in the region between 4000–5700 Å, we restrict the fit to this region.

The continuum plus Fe II emission were fit using Equation 1:

$$F(\lambda) = F_{\lambda}^{PL} + (F_{\lambda}^{\text{FeII}} * G_{\lambda}) \quad (1)$$

Where $F_{\lambda}^{PL} \propto \lambda^{\alpha}$ describes the power law, and $F_{\lambda}^{\text{FeII}}$ represents the [Boroson & Green \(1992\)](#) Fe II template convolved with a Gaussian kernel, G_{λ} , in velocity space, $V_{\text{FeII}} = \sqrt{V_{\text{temp}}^2 + V_{\text{conv}}^2}$. To fit the continuum and the emission lines (see next section) we used our own python code, which makes use of the SCIPY library and the `curve_fit` function. All fitting procedures in this work use this python function to estimate the best parameters in each case, obtained by minimization of the χ^2 along the spectral region of the fit, masking the emission lines H β , [O III] λ 4959,5007 and H γ . The final model, its components and the pure emission line spectrum resulting from its subtraction can be seen in middle panel of Figure 2.

To model the continuum in the UV we used a single power law function, F_{λ}^{PL} . The Fe II emission, if present, is at the continuum level and blended to the noise of the spectrum. We found a power law index of -1.2 , consistent with the optical counterpart of the PHL 1092 spectrum. The bottom panel of Figure 2 shows the modeled continuum and the pure emission lines spectrum. Prominent lines present in the spectrum are Ly α , C IV λ 1549, C III λ 1909, Al III λ 1860, and Si III λ 1892.

The NIR continuum were modeled using similar approach to that of the optical region. However, it was necessary to include a third component to account for the excess of continuum emission over the underlying power-law component redwards of $\sim 1\mu\text{m}$, attributed to dust heated by the AGN ([Landt et al. 2008](#)). Thus, a three component model were used for this purpose: (i) The same power-law observed in the optical, extended to the NIR; (ii) the [Garcia-Rissmann et al. \(2012\)](#) template for the NIR Fe II pseudo-

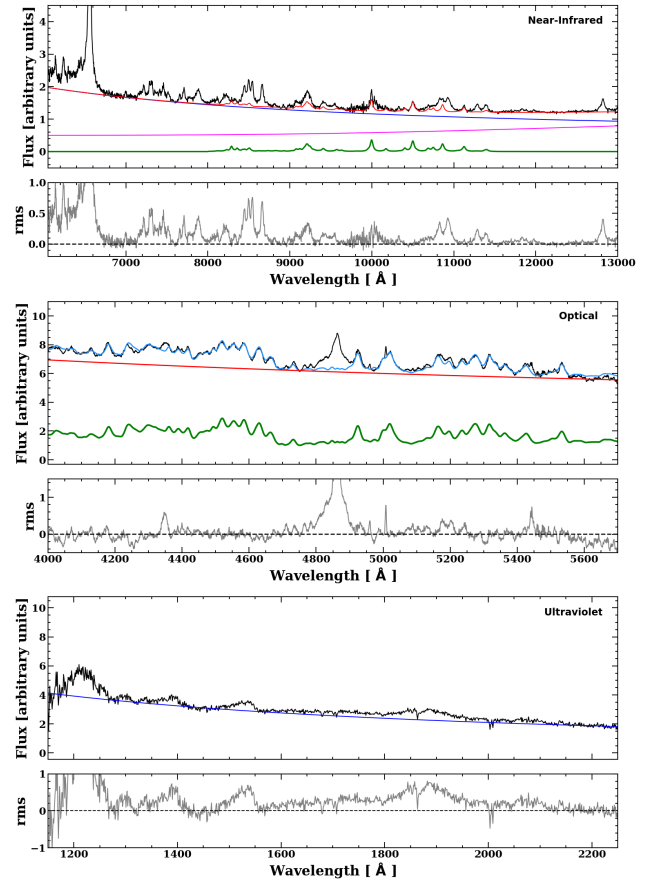


Figure 2. Continuum components in the optical and NIR spectra of PHL 1092 (shown in black). Top panel: NIR region of the spectrum. The power law, black body, and Fe II template composing the continuum of the source are shown in blue, magenta and green lines, respectively. The sum of these components is shown in red. Middle panel: optical region of the spectrum. The power law and Fe II emission are shown in red and green, respectively. The best model is shown in cyan. Bottom panel: UV region of the spectrum. Blue line shows the power law fitted to the spectrum. In all panels, the bottom part of the panel shows the ‘pure emission line’ spectrum (in grey), with the Fe II and continuum subtracted.

continuum; and (iii) a black body function, to account for the dust emission. This model is represented by equation 2:

$$F(\lambda) = F_{\lambda}^{PL} + F_{\lambda}^{\text{BB}} + (F_{\lambda}^{\text{FeII}} * G_{\lambda}) \quad (2)$$

where $F_{\lambda}^{PL} \propto \lambda^{\alpha}$ is the power law, $F_{\lambda}^{\text{BB}} = B_{\lambda}(T)$ is a Planck function for the warm dust, $F_{\lambda}^{\text{FeII}}$ is the [Garcia-Rissmann et al. \(2012\)](#) template broadened by convolving it with a kernel, G_{λ} , using as reference the width (in velocity space) of the line Fe II λ 10502, the strongest isolated Fe II line in the NIR. The best fitted model, the individual components and the residual emission line spectrum are plotted in the top panel of Figure 2.

The FWHM of the kernel employed to convolve the NIR template was 1150 km s^{-1} , consistent with the value of 1200 km s^{-1} obtained for the optical template. Moreover, the power law index obtained for the optical and NIR are 1.26 and 1.39, respectively. Within uncertainties, they are consistent, implying that we are indeed observing in the NIR

the optical extension of the continuum associated to the central source. The small difference between these two values is probably due the missing part of the spectrum, which introduces a small uncertainty in the individual slopes. Finally, the black body temperature obtained from the fit was 1290 K, which is consistent with the temperature of warm dust found in AGN (Granato & Danese 1994; Rodríguez-Ardila & Mazzalay 2006), close to the sublimation temperature of the dust grains, ~ 1600 K.

From figure 2, we see that the Fe II template suitably reproduces the optical Fe II. There have been claims in the literature that a narrow component of Fe II could also contribute to the emission in this spectral region (Véron-Cetty et al. 2004; Bruhweiler & Verner 2008; Dong et al. 2010). The models from Bruhweiler & Verner (2008) imply that a significant part of Fe II bump at 4570 \AA could be produced by a narrow system of Fe II lines. Dong et al. (2010), using template modeling, found residual narrow Fe II emission in a SDSS sample of NLS1, although much weaker than the broad component. They also noticed that narrow permitted Fe II lines are completely absent in Seyfert 2 galaxies. We did not identify residual narrow Fe II lines neither in the optical nor in the NIR spectrum of PHL 1092. If this narrow component is present, it should be visible, at the very least, in the isolated NIR Fe II lines such as Fe II $\lambda 10502$ and Fe II $\lambda 11127$ after subtraction of the broad component. We therefore conclude that the strength of a putative contribution of a narrow component to the Fe II spectrum should be negligible.

Three features, though, call the attention in the NIR pure emission line spectrum: the broad emission line around $\lambda 9200$, the small bump redwards of He I $\lambda 10830$, and a set of unidentified lines at $\lambda 11400$.

In order to search for their origin, we should recall first that the Fe II template of Garcia-Rissmann et al. (2012) was constructed based on the models of Sigut & Pradhan (2003) with modifications in some multiplet strengths to match the spectrum of I Zw 1. The three features mentioned above were, in fact, modified during the construction of the template. Since PHL 1092 is a super-strong Fe II emitter, it is very likely that these features had their intensities underestimated from the template derived from I Zw 1. In this context, the observed excess of emission at 9200 \AA , 10800 \AA and 11400 \AA is genuine and not properly modeled by the Garcia-Rissmann et al. (2012) template (see next section). Note, however, that the residual bump redward of He I could also be due to an additional broad component of that line. If this hypothesis is correct, we should also detect a similar broad component (in FWHM and relative position from the rest-wavelength of the line) in Pa β , which is not the case. We conclude that the Fe II transitions leading to the emission lines at 9200 \AA , 10800 \AA and 11400 \AA are enhanced in PHL 1092. In order to confirm whether that excess of Fe II emission is common in extreme Fe II emitters, a larger sample of such objects would be necessary.

3.2 The BLR spectrum of PHL 1092

The fit described in the previous section allowed us to remove from the observed optical to NIR spectrum the continuum emission due to the central source and the Fe II pseudo-continuum. The pure nebular spectrum is clearly

dominated by low ionization lines such as O I, Ca II, and H I emitted in the BLR. Narrow forbidden emission lines such [Fe II] $\lambda 12570$, [O III] $\lambda 4959$ and [S III] $\lambda 9531$ are rather faint. In the UV spectra, emission lines of He II, C IV, Al III, S III], C III], Si IV and O IV] were identified. Parameters of the broad lines (flux and width) were derived assuming that the line profiles can be represented by a single or a combination of Lorentzian or Gaussian functions. The best solution was obtained when the reduced χ^2 of the fit reaches the minimum value. All line widths presented here were corrected for instrumental broadening using $FWHM(real)^2 = FWHM(observed)^2 + FWHM(instrumental)^2$, where FWHM(instrumental) is 360 km s^{-1} , 180 km s^{-1} and 80 km s^{-1} for GNIRS, Goodman and STIS, respectively.

The UV spectrum of PHL 1092 has three main features that carry important information about the BLR: Si IV, C IV, and the blend around 1900 \AA , formed by the contribution of different species (see below). Since PHL 1092 has a strong Fe II emission and narrow broad lines, it is classified as a population “A” AGN. In such type of sources, the broad lines profiles are better represented by a Lorentzian function. The emission line at 1400 \AA is actually a blend of Si IV $\lambda 1397 + \text{O IV}] \lambda 1402$ (Martínez-Aldama et al. 2018a). We fit that feature using two Lorentzians to represent the rest-frame component of the blend, and a combination of two Gaussians profiles to represent the blue asymmetry observed in the line. The C IV line were fit using a Lorentzian with the addition of two Gaussians to account for the blue asymmetry, usually associated to outflows (Coatman et al. 2016). This approach in both fits warrants a proper modeling of the asymmetry without *ad-hoc* assumptions about its origin. The flux and the FWHM of these lines are listed in Columns 2 and 3, respectively, of Table 1 and the best fit with the individual components can be observed in Figure 3 (a) and (b). Note that the broad components of C IV, Si IV, and O IV] are especially uncertain due to the much stronger emission of the Blue component. For that reason, the fluxes associated to the broad components of these lines are marked with a “:”. We also measured the specific flux in a small range at $\approx 1400 \text{ \AA}$ and at 1549 \AA where we expect the rest frame component emission of Si IV, and C IV], respectively. We obtain $5 \cdot 10^{-16} \text{ erg s}^{-1} \text{ cm}^{-2} \text{ \AA}^{-1}$ for Si IV and $3 \cdot 10^{-16} \text{ erg s}^{-1} \text{ cm}^{-2} \text{ \AA}^{-1}$ for C IV. The ratio Si IV / C IV is therefore ≈ 1.7 , consistent with the ratio reported in Table 2.

The blend at 1900 \AA is composed of Fe II, Fe III, C III] $\lambda 1909$, Si III] $\lambda 1892$, and Al III $\lambda 1860$. We follow the procedure outlined in Martínez-Aldama et al. (2018a) to fit this bump. First, we used the Vestergaard & Wilkes (2001) UV Fe II+Fe III template with Lorentzians profiles to model the last three lines. Note that Al III $\lambda 1860$ is actually a doublet at $\lambda \lambda 1854, 1862$, with equal intensity (1:1). We found that Si III] and C III] has a prominent blueshifted component, which according to Martínez-Aldama et al. (2018a) is rare although observed before in even more extreme regimes than that observed in PHL 1092 (Martínez-Aldama et al. 2018b). We modeled the blueshifted components with a Gaussian profile. The corresponding FWHM, fluxes and line shifts are listed in Table 1. The best fit can be observed in Figure 3 (c). Table 2 provides UV line ratios relevant to the classification (PHL 1092 meets the “extreme Population A” criteria of

Marziani & Sulentic 2014), and to the tentative definition of the BLR physical conditions (Sect. 4.3).

We fit $H\alpha$ and $H\beta$ with Lorentzian profiles, representing the BLR contribution. In addition, we noticed a blue asymmetry in these lines, which was fit with a Gaussian component, following the approach of Negrete et al. (2018). Moreover, we employed one Gaussian to model each of the $[O III]\lambda\lambda 4959, 5007$ doublet. We did not find evidence of the $[N II]$ doublet around $H\alpha$. Note that the $[S III]\lambda 9531$, usually the strongest NIR narrow forbidden line (Landt et al. 2008; Riffel et al. 2006; Mason et al. 2015), was not detected in our spectrum, suggesting that the NLR contribution is likely below the detection limit of the spectrograph. The lack of $[N II]$ and $[S II]$ detection is consistent with the weakness of $[S III]$ and $[O III]$. Since the $[O III]$ and $[S III]$ are usually the strongest narrow lines in the optical and NIR, respectively, and $[N II]$ and $[S II]$ are just a fraction of $[O III]$ (~ 0.3), it is not expected that they show up in the spectrum. The panels (d) and (e) of Figure 3 show the best fit for $H\beta$ and $H\alpha$, respectively. The parameters of the fit are listed in Table 1. Moreover, the Fe II emission bump centered in $\lambda 4570$ was measured using the template fit in the previous section. The flux labeled Fe II (4570 Bump) presented in Table 1 is the integrated flux of the bump in the wavelength interval 4434–4684 Å (Boroson & Green 1992).

The $O I \lambda 8446$ and the $Ca II$ triplet ($\lambda 8496$, $\lambda 8542$, and $\lambda 8663$) were fitted considering two constraints. First, $O I \lambda 8446$ was constrained to have the same FWHM (in velocity space) as $O I \lambda 11297$. Second, $Ca II \lambda\lambda 8496, 8542$ and $\lambda 8663$ were constrained to have the same width (Rodríguez-Ardila et al. 2002). The values obtained are listed in Table 1 and the fit is presented in Figure 3(f).

The bump at 9200 Å is a blend of Fe II and Pa9. Marinello et al. (2016) showed that the NIR Fe II template usually underestimates the total flux in that feature. The residual emission left after subtraction of the template is composed of the residual contribution of Fe II and the Pa9 line. In order to obtain a more accurate measurement of the Fe II emission in the bump we followed the technique presented by Marinello et al. (2016), which consists of subtracting the Pa9 contribution to the bump after scaling down $Pa\gamma$ by the theoretical $Pa\gamma/Pa9$ ratio (Case B). After this subtraction, the residual should consist of a pure Fe II emission, which can be fit with a proper function (Lorentzian in this case). The total flux of the bump is the sum of the fluxes from the template added to that the residual (see Table 1). Figure 3(g) shows the fit applied to this region.

The only prominent Paschen line detected in the spectrum is $Pa\gamma$, which is moderately blended with $He I \lambda 10830$. Other Paschen lines fall in the region of poor atmospheric transmission. We model the above two lines with a Lorentzian profile, representing the broad component. No narrow component was detected above 3σ level. The FWHM of the broad components of $Pa\gamma$ and $He I$ are 1900 and 1850 km/s, respectively. The value found for $Pa\gamma$ is consistent to that measured in $H\beta$, showing that the results found are robust. The best fitted profiles can be seen in panel (h) of Figure 3.

The $O I \lambda 11297$ and $Fe II \lambda 11400$ were also fitted using a Lorentzian function. Both features are slightly blended. This function most suitably represents the shape of these lines compared to a Gaussian function and is consistent with

the profile fit to $H\beta$. Note that $Fe II \lambda 11400$ was subtracted using the Fe II template but it was significantly underestimated by it, leaving a strong residual emission feature. We estimate the total flux in $Fe II \lambda 11400$ by summing the flux value obtained from the template and that of the additional component fit to the residuals. Figure 3(i) shows the fit to $O I \lambda 11287$ and $Fe II \lambda 11400$. The integrated flux and FWHM are also presented in Table 1.

Another important Fe II features in the NIR are the so-called 1 μm lines, e.g., $Fe II \lambda\lambda 9998, 10502, 10863$ and 11127 Å. We measured the flux of these lines directly from the fit carried out using the Garcia-Rissmann et al. (2012) template. The results for each individual line is presented in Table 1. For all lines measured in this work we list in the same table the integrated signal-to-noise (S/N) and the line shifts with respect to the systemic velocity of the galaxy in Columns 4 and 5, respectively.

4 DISCUSSION

4.1 PHL 1092 in the Eigenvector 1 context

It has been 27 years since Boroson & Green (1992) presented their seminal work that shows that most of the spectral features of an AGN can be parameterized in terms of two variables, called Eigenvector 1 (E1). They showed that the anti-correlation between the flux ratio $Fe II_{4570}/H\beta$ and the EW of $[O III]$ forms an optimal parametric space where several other properties relates with. This concept was later extended by Sulentic et al. (2000c) to a four-dimensional parameter space, 4DE1, where the $FWHM(H\beta)$, R_{4570} , the shift of the peak of C IV relative to the systemic velocity, and the photon spectral index of the soft-Xray power-law Σ , were added. The main physical driver of the E1 has been attributed to variations of the accretion rate among different AGN (Boroson 2002; Marziani et al. 2001; Shen & Ho 2014) while the spread of the $FWHM(H\beta)$ in the optical is probably related to orientation effects (Shen & Ho 2014).

In order to include PHL 1092 in the E1 diagram it is necessary to estimate its corresponding R_{4570} . Using the values measured in the previously section (see Table 1), we estimate $R_{4570}=2.58$. The Fe II emission in AGN can be divided into basically three categories. Weak Fe II emitters, with $R_{4570} < 1$, strong Fe II emitters, with $1 < R_{4570} < 2$, and super-strong Fe II emitters, with $R_{4570} > 2$. Typical AGN are weak Fe II emitters, with $\sim 90\%$ of them in this category, and highly concentrate around $R_{4570} \sim 0.6 - 0.8$ (Shen & Ho 2014). Strong Fe II emitters are less common, occurring in about 5% of the AGN population (Lawrence et al. 1988). Super-strong Fe II emitters are even more rare, roughly an order of magnitude less (Mooran et al. 1996; Lipari et al. 1993). In this scheme, PHL 1092 is in the category of super-strong Fe II emitters.

Bergeron & Kunth (1980) were the first to identify PHL 1092 as a super-strong Fe II emitter. They showed that the optical spectrum was dominated by intense Fe II lines and that such emission could only arise from gas of high electronic density, $n_e \sim 10^{12} \text{ cm}^{-3}$, and low temperature, $T \sim 10000 \text{ K}$. However, the value of R_{4570} they reported was surprisingly high, $R_{4570}=6.2$, making PHL 1092 the strongest Fe II emitter ever identified. Lawrence et al. (1997) proposed

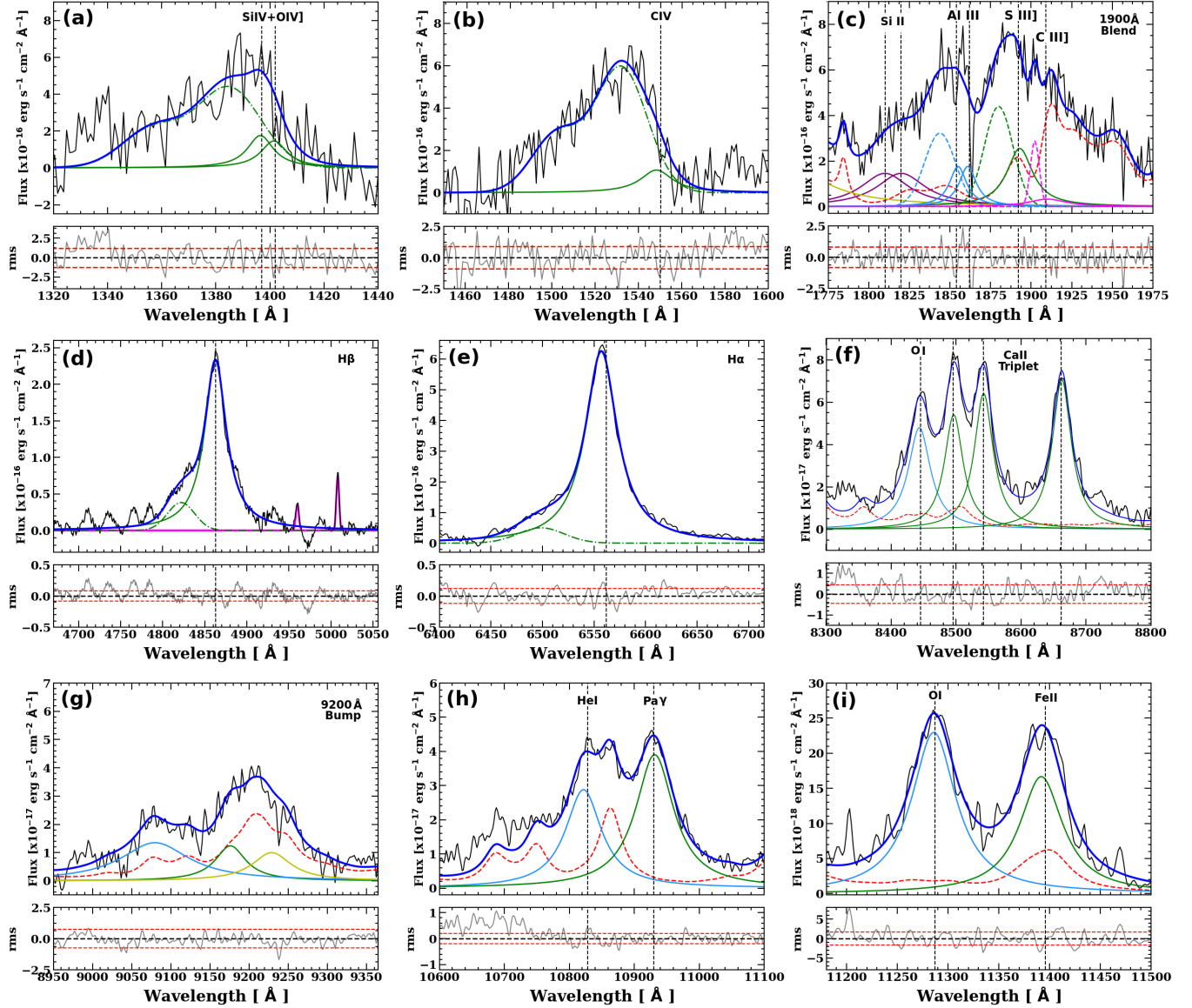


Figure 3. Line fit of all lines of interest for this work. Panel (a) shows the 1400 Å complex, which consist of the Si IV λ 1397+O IV λ 1402 broad lines (solid green) and a blueshifted component (dashed green). Panel (b) shows the C IV line. The broad line was fitted using a Lorentzian (solid green) added with two Gaussians to model its blueshifted component (dashed green). Panel (c) shows the 1900 Å blend. The broad components of C III λ 1909, Si III λ 1982, Al III λ 1860, and S II λ 1812 are denoted by the magenta, green, pale blue, and purple solid lines, respectively. The blueshifted components of each line are shown in dashed lines of same color. The yellow solid line shows part of the red wing of Ni III λ 1750. Panel (d) shows the H β line and the blueshifted component are shown in green solid and dot-dashed lines, respectively, and the [O III] lines are shown in magenta. Panel (e) shows the H α line fit. The solid and dot-dashed green lines show the broad component and the blueshifted component, respectively. Panel (f) plots the O I + Ca II triplet region. The O I is shown in pale blue and the Ca II triplet is shown in green. Panel (g) shows the 9200 Å Fe II bump. The solid yellow line shows the Pa9 line, and the solid green and pale blue lines shows the complementary Fe II lines introduced to obtain the missing Fe II flux in the bump. Panel (h) shows the He I λ 10830 (pale blue), the Pa γ lines (green). Panel (i) shows the O I λ 11287 (solid pale blue line) and the Fe II feature at 11400 Å (solid green line). In all panels the bold blue line shows the complete fit of all components, observed spectrum in black and the Fe II + Fe III template in dashed red.

that values of R_{4570} in the interval 4-8, published in the literature by Joly (1991), could be too high. They indeed found for PHL 1092 a R_{4570} of 1.8.

The large discrepancies in the value of R_{4570} found here and those in the literature are likely due to the method employed to measure the flux contained in the Fe II bump. In Bergeron & Kunth (1980), most of the flux redwards of H β was associated to Fe II multiplets, reducing the amount of

H β flux in the broad Lorentzian wings of the line profile and thereby increasing R_{4570} to higher values. The continuum level set in the measurements is also a factor that can lead to a smaller value of R_{4570} . Figure 2 shows that a flat continuum under the Fe II λ 4570 bump would underestimate the integrated flux of that feature. The value of R_{4570} presented here is based on a simultaneous fit to the continuum and the Fe II spectrum observed in the UV/optical region,

Table 1. Emission line fitting results.

Line	Flux ($\times 10^{-16}$ erg s $^{-1}$)	FWHM (km s $^{-1}$)	Integrated S/N	Line shift ^a (km s $^{-1}$)
H β _{BC}	112.01 \pm 2.43	1850 \pm 100	46	0
H β _{Blue}	21.85 \pm 1.85	2300 \pm 200	8	-2470
[O III] λ 4959	1.58 \pm 0.30	300 \pm 50	3	0
[O III] λ 5007	3.13 \pm 0.35	300 \pm 50	5	0
H α _{BC}	363.58 \pm 4.15	1715 \pm 100	116	-218
H α _{Blue}	28.11 \pm 1.18	2350 \pm 210	6	-2700
O I λ 8446	31.26 \pm 1.90	1350 \pm 100	23	-95
Ca II λ 8495	29.47 \pm 1.85	1250 \pm 120	23	0
Ca II λ 8543	35.12 \pm 1.84	1250 \pm 120	29	0
Ca II λ 8662	29.23 \pm 1.90	1250 \pm 120	31	0
Fe II λ 9998	24.90 \pm 2.20	1150 \pm 75	–	0
Fe II λ 10502	23.14 \pm 0.90	1150 \pm 75	25	0
He I _{BC} λ 10829	30.25 \pm 1.50	1860 \pm 150	26	-219
Fe II λ 10863	22.315 \pm 0.90	1150 \pm 75	23	0
Pa γ _{BC}	43.53 \pm 2.00	1900 \pm 130	35	0
Fe II λ 11127	13.10 \pm 1.12	1150 \pm 75	20	0
O I λ 11287	19.06 \pm 1.45	1350 \pm 100	23	-55
Fe II λ 11400	18.21 \pm 1.10	1150 \pm 75	23	-105
Si IV λ 1397	32:	2500 \pm 150	3	-101
O IV] λ 1402	27:	2500 \pm 150	3	-106
Si IV+O IV]Blue	186.84 \pm 17.15	9400 \pm 1030	17	-4700
C IV λ 1549	30:	3800 \pm 175	4	-184
C IV _{Blue}	255.11 \pm 22.93	5350 \pm 295	10	-3500
C III] λ 1909	14.51 \pm 1.02	4200 \pm 315	3	0
C III]Blue	29.35 \pm 1.78	1800 \pm 115	7	-1100
Si III] λ 1892	76.64 \pm 5.29	3100 \pm 150	12	0
Si III]Blue	141.25 \pm 12.67	3400 \pm 160	23	-1750
Al III λ 1860 ^b	70.06 \pm 1.12	2150 \pm 175	9	0
Al III _{Blue}	111.27 \pm 17.12	3700 \pm 175	20	-950
Fe II (4570 Bump)	288.55 \pm 10.3	–	–	–
Fe II (9200 Bump)	79.50 \pm 1.12	–	–	–
Fe II (1 μ m lines)	79.53 \pm 1.75	–	–	–

^a Negative values are regarded as blueshifts

^b Summed flux of the lines in the doublet

Table 2. Broad emission line ratios.

Line Ratio	Value
R ₄₅₇₀	2.58 \pm 0.13
R ₉₂₀₀	1.02 \pm 0.10
R _{1μm}}	1.02 \pm 0.11
Al III/Si III]	0.91 \pm 0.09
C III]/Si III]	0.19 \pm 0.07
Si IV+O IV]/Si III]	0.76:
C IV/Al III]	0.42:
C IV/Si III]	0.39:
Si IV+O IV]/C IV	1.94:
(Si IV+O IV)]/C IV ^a	0.86 \pm 0.09

^a Ratio between the summed flux of BC and Blue.

resulting in more robust approach. In order to compare the different values reported in the literature with ours, we show in Figure 4 our spectrum and template, and how it would look if the R₄₅₇₀ were 1.8 and 6.2. As shown in Figure 4, a

R₄₅₇₀ of 6.2 is unrealistic, being the value of R₄₅₇₀= 2.58 far more suitable to the observations.

The other axis of the E1 plane is the FWHM of H β , FWHM(H β). The value obtained for the broad component is 1850 km s $^{-1}$, consistent with the classification of PHL 1092

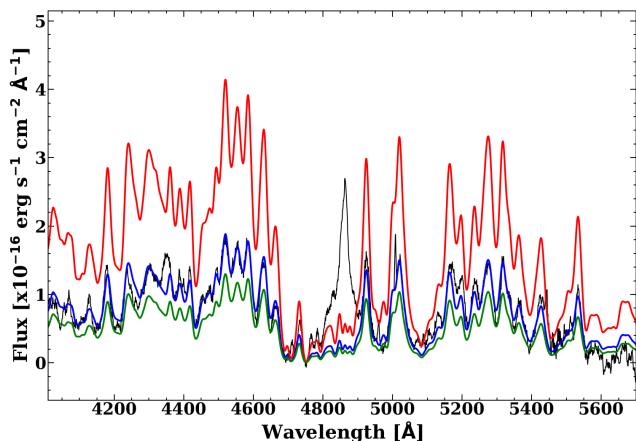


Figure 4. PHL 1092 with the Fe II template scaled to the different values of R_{4570} from the literature. The observed spectrum with the power law subtracted is shown in black. The best fitted Fe II template in this work are shown in blue. The red and green lines show the template scaled to reproduce the R_{4570} obtained by Bergeron & Kunth (1980), $R_{4570}=6.2$, and by Miniutti et al. (2012), $R_{4570}=1.8$, respectively.

as a NLS1 AGN. It also places PHL 1092 in the “population A” region of the E1 optical plane (Marziani et al. 2001), as shown in Figure 5. In that plot, grey points represent the sources from Sulentic et al. (2007), green triangles are those of Lipari et al. (1993) and blue squares are AGN are from Śniegowska et al. (2018). PHL 1092 is represented by the red star. Even after reducing the estimate of R_{4570} for PHL 1092, it still remains as outstanding source.

Other objects with super-strong Fe II emission were presented by Lipari et al. (1993): IRA07598+6508, Mrk 231, Mrk 507, and IRAS18508-7815. All of them with $R_{4570} > 2$. Shen & Ho (2014), analyzing the physical drivers of EV1, derived the same diagram for all SDSS (DR7) sources from Shen et al. (2011). An immediate result from their work is the lack of sources with $R_{4570} > 3$. In fact, in their E1 diagram, it is possible to see an upper R_{4570} cutoff around $R_{4570} \sim 2.2$. Śniegowska et al. (2018) re-analyzed 27 of the strongest Fe II emitters ($R_{4570} > 1.3$) from the Shen et al. (2011) catalog. Their results show that many sources in Shen et al. (2011) had their R_{4570} overestimated, very likely due to the automated procedure employed to derive this quantity and the low S/N of some of the spectra. That is the case of SDSS125343.71+122721.5, which has $R_{4570}=1.75$ in Shen et al. (2011) but is reported with negligible Fe II emission in Śniegowska et al. (2018). They also identified another outstanding source of Fe II emission, SDSS125343.71+122721.5. This AGN has a $R_{4570}=2.12$ in Shen et al. (2011) catalog and after Śniegowska et al. (2018) analysis, they presented two different values: (i) $R_{4570}=3.0$ and $FWHM(H\beta)=1445 \text{ km s}^{-1}$ for a Gaussian profile to fit $H\beta$, and (ii) $R_{4570}=2.12$ and $FWHM(H\beta)=936 \text{ km s}^{-1}$ using a Lorentzian profile instead.

Similarly, Negrete et al. (2018) analysed a sub-sample of 302 AGN up to redshift 0.8 and Eddington ratio close to 1, extracted from the much larger sample of Shen et al. (2011). In their work they found that these sources are characterized

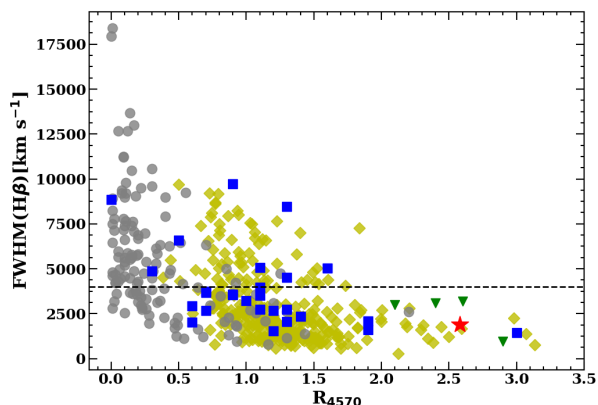


Figure 5. Eigenvector 1 optical plane. The red star shows PHL 1092. The other super-strong Fe II emitters from Lipari et al. (1993) are plotted in green triangles. High Eddington ratio AGN from Negrete et al. (2018) are denoted by yellow diamonds. The sources which had their R_{4570} re-estimated by Śniegowska et al. (2018) are shown in blue squares. The grey circles show the sources in Sulentic et al. (2007). The black dashed line show the separation in $FWHM(H\beta)$ of ‘Population A’ and ‘Population B’.

by strong Fe II emission. In particular, it was found that 16 sources have $R_{4570} > 2$, with 5 of them displaying $R_{4570} > 2.5$.

The higher values of R_{4570} are sometimes due to the very narrow profile of $H\beta$. In these extreme NLS1 galaxies, the $H\beta$ line is dominated by a narrow component. The distinction between the contribution from the BLR and NLR are extremely subtle and, in some cases, can only be fully evaluated by means of multi-wavelength spectra (i.e. optical and NIR data). Therefore, a careful fit to the $H\beta$ region, taking into account the power-law continuum and simultaneously the Fe II emission, is crucial to derive consistent values of R_{4570} .

Zamanov et al. (2002) pointed out that in Population A of AGN, strong Fe II emitters with narrow $H\beta$ profiles tend to have a large blueshifted component in [O III]. This trend, though, is not observed in PHL 1092. This may be due to an intrinsic effect caused by the low strength of the [O III] lines. This is in agreement with Boroson & Green (1992) and Shen & Ho (2014), who found a negative correlation between the intensity of [O III] and the strength of the Fe II. As the blueshifted [O III] component is usually weaker than the main narrow component, if the former is present, it is probably below our detection limit or heavily blended with the adjacent Fe II features. A higher spectral resolution spectrum is indeed necessary to uncover the presence of such outflow component.

Another implication of the E1 is that strong Fe II emitters should host low black hole masses and high Eddington ratio (Negrete et al. 2018). In order to estimate the black hole mass in PHL 1092, M_{BH} , we used Vestergaard & Peterson’s (2006) single epoch black hole mass equation:

$$\log(M_{BH}) = \log \left\{ \left[\frac{FWHM(H\beta)}{10^3 \text{ km s}^{-1}} \right]^2 \left[\frac{\lambda L_{\lambda}(5100)}{10^{44} \text{ erg s}^{-1}} \right]^{0.5} \right\} + (6.91 \pm 0.02)$$

(3)

For PHL 1092 we measured a $\text{FWHM}(\text{H}\beta) = 1850 \text{ km s}^{-1}$ and $L_\lambda(5100) = 1.497 \times 10^{41} L_\odot$. It translates using Eq. 3 in a black hole mass of $\log(M_{\text{BH}}) = 7.89 M_\odot$. Other works in the literature report different values of M_{BH} for PHL1092. For instance, Dasgupta et al. (2004) using optical scaling relation for the BLR radius and single epoch method found $\log(M_{\text{BH}}) = 8.20 M_\odot$. Czerny et al. (2001) found $\log(M_{\text{BH}}) = 6.09 M_\odot$ using X-ray variability and $\log(M_{\text{BH}}) = 8.26 M_\odot$ from accretion disk fitting method. Nikolajuk et al. (2009) found $\log(M_{\text{BH}}) = 8.46 M_\odot$ using more recent scaling relations for the optical single epoch recipe. By the same method, Miniutti et al. (2012) found $\log(M_{\text{BH}}) \sim 8.48 M_\odot$. From x-ray observations, and considering a non-spinning BH Miniutti et al. (2012) found a $M_{\text{BH}} = 8.38 M_\odot$, consistent with their optical measurement. Our result is only factor 1.2 lower than the average of previous values presented in literature. However, note that they estimate the M_{BH} using different methods and scaling relations. Moreover, the black hole mass obtained here for PHL 1092 is consistent with the average of masses obtained by Rakshit et al. (2017) and Negrete et al. (2018). The Eddington ratio is defined by the ratio between the bolometric luminosity and the Eddington limit, e.g., $L/L_{\text{Edd}} = L_{\text{bol}}/L_{\text{Edd}}$, where $L_{\text{Edd}} = 1.5 \times 10^{38} (M_{\text{BH}}/M_\odot)$ (Netzer & Marziani 2010). The bolometric luminosity can be obtained applying a correction factor to the optical luminosity measured from the continuum at 5100\AA , $L_{\text{bol}} = c \times \lambda F_\lambda(5100\text{\AA})$, where $c=7$ (Netzer & Trakhtenbrot 2010). We estimate a $\log(L_{\text{bol}}) = 45.72 \text{ erg s}^{-1}$ and $L/L_{\text{Edd}} = 1.24$. Negrete et al. (2018) using a sample of 334 high Eddington ratio AGN found that strong Fe II emitters ($R_{4570} > 1$) are associated with high L/L_{Edd} . Our results presented above show that PHL 1092 follows this same trend, having a high accretion rate and M_{BH} typical of Population A AGN. Despite the number of sources with $R_{4570} > 2$ is much smaller than weaker Fe II emitters, those analyzed by Negrete et al. (2018) and here suggest that indeed these characteristic are common to all extreme Population A AGN.

4.2 The Fe II Emission Region

The Fe II emission arises from clouds located in the broad line region, which is unresolved even for closest AGN at sub-arcsec resolution observations. For this reason, the structure and location of the gas where these lines are produced must be derived using integrated spectra. Better estimates of the BLR structure can be achieved using reverberation mapping. Indeed, studies focused on variability have detected Fe II time lags for a few AGN (Rafter et al. 2013; Barth et al. 2013; Du et al. 2016). The main result gathered from these works is that the clouds emitting Fe II are located at distances that coincide with that of the H β emission region and up to twice that from the central source. However, no consensus regarding the precise location of the Fe II emission region has been achieved.

In order to get clues about the possible location of the Fe II emitting region in PHL 1092 we plot in Figure 6(a) the FWHM of Fe II versus the FWHM of O I and Ca II from the sample of Marinello et al. (2016). We add the value of PHL 1092 as a red star for comparison. The results show that the FWHM of these lines follow a similar distribution,

being slightly scattered around the identity line. Under the virial assumption, the relative values of the line widths can be used as a proxy of the distance ratios from the central source, providing a relative location of the emitting region if variations in FWHM for different ions within the same object are detected. In this context, Figure 6(a) shows that Fe II, O I, and Ca II in PHL 1092 are likely formed in gas that is co-spatial, at the same distance from the AGN.

Similar results were already reported in the literature. For instance, Rodríguez-Ardila et al. (2002) studying the physical process behind the O I emission lines found that Fe II and O I lines share the same profile shape, and very similar FWHM. Using a similar argument, Matsuoka et al. (2007) and Martínez-Aldama et al. (2015) employed the O I emission line to probe the physical conditions of the emitting region of O I and Fe II. They all agree that these lines are formed in a same portion of the BLR, in dense clouds ($n_{\text{H}} > 10^{11.5} \text{ cm}^{-3}$) illuminated by a ionizing radiation of $U < 10^{-2.5}$. Moreover, Matsuoka et al. (2008) compiled O I and Ca II line properties of 11 quasars in a broad range of redshift and luminosity ($0.06 < z < 1.08$ and $-29.8 < M_B < -22.1$) in order to analyze the physical conditions that lead to the production of these lines. They found that the widths of the O I were remarkably similar over more than 3 orders of magnitude in luminosity, suggesting a similar kinematics for location of the emission region. They also argue about the dust presence and suggest that the emission region should be located near the dust sublimation point at the outer edge of the BLR. Thus, the results for PHL 1092 in Figure 6(a) suggests that Fe II is formed in outer portion of the BLR.

In contrast, the hydrogen lines are likely to be produced closer to the central source. Figure 6(b) shows the FWHM of Fe II versus the FWHM of Pa β (Pa γ for PHL 1092). We see that the FWHM of Pa β is systematically broader than that of Fe II. For PHL 1092, the FWHM of H β is about $\sim 60\%$ larger than that of Fe II (and the other low-ionization lines analyzed, e.g., O I and Ca II). From the virial theorem, we have that the distance $D \propto 1/\text{FWHM}^2$, which translates in a Fe II emission region 2.5 times more distant than that where the bulk of Hydrogen lines are produced. Marinello et al. (2016) obtained an averaged FWHM for Fe II that is 3/4 smaller than that of Pa β . In particular, for IZw1, the strongest Fe II emitter of their sample, the results are quite similar to PHL 1092, with the $\text{FWHM}(\text{Fe II}) = 1/2 \text{ FWHM}(\text{Pa}\beta)$.

Our results are also consistent with the BLR scenario proposed by Dultzin-Hacyan et al. (1999). Their BLR model interpret the observed C IV as a radial outflow from the central source while low ionization species, such as Fe II and Ca II, arise in the outer portion of the BLR. The intensity and blueshift of C IV in this case would depend on the observing angle. In this scenario C IV would be produced in a ‘‘cone shaped’’ inner region. The results for the FWHM(C IV) and strong blueshifted component, narrower Fe II, O I, and Ca II profiles measured not only in PHL 1092 but in a larger sample of objects (Marinello et al. 2016) agree with this scenario.

Note that in the above analysis we did not consider any effects between ionization potential of the ion, FWHM and location of the emitting region as is usually considered for C IV and Hydrogen lines because all the lines here have very similar ionization potential, $\leq 13.6 \text{ eV}$.

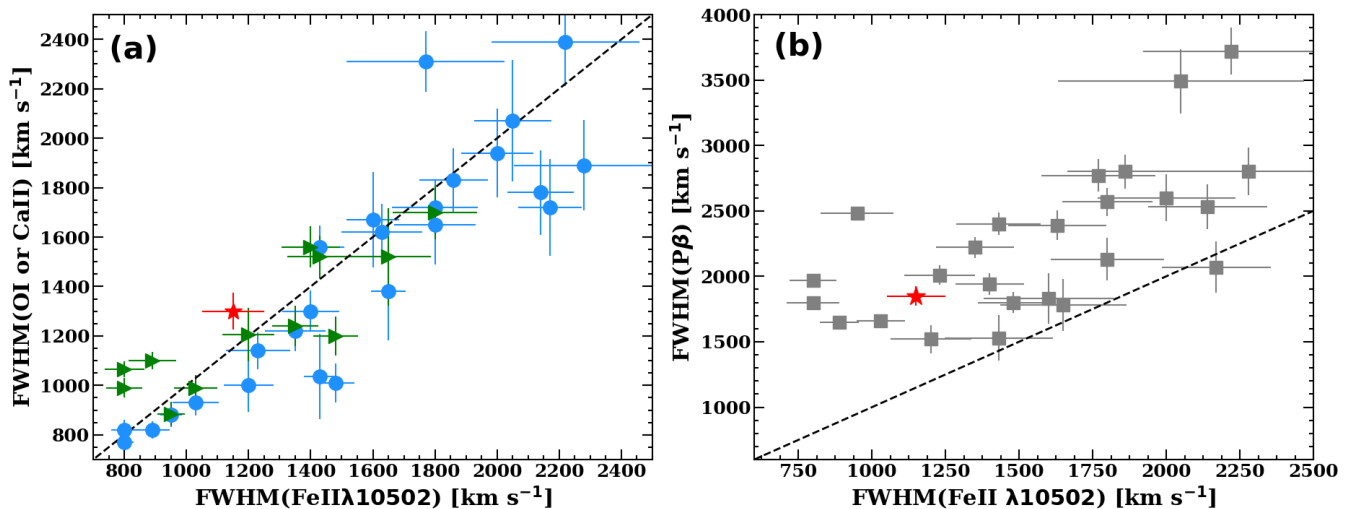


Figure 6. Correlation between the FWHM of the low ionization lines. Panel (a): FWHM(OI λ 1127) (blue squares) and FWHM(Ca II λ 8662) (green triangles) plotted against the FWHM(Fe II λ 10502), the most prominent isolated Fe II line, using the sample of [Marinello et al. \(2016\)](#). Panel (b): FWHM(P $\alpha\beta$) against FWHM(Fe II λ 10502) is plotted in grey squares of the [Marinello et al. \(2016\)](#) sample. In both panels the black dashed line is the identity function and the PHL 1092 is denoted by the red star.

4.3 Physical conditions within the BLR

Besides the region where the Fe II emitting clouds is located relative to the central source, we can also estimate its physical conditions within the BLR. The line fluxes from the NIR and UV spectra derived in section 3.2 can be used in combination with CLOUDY simulations to constrain the physical properties of the BLR gas such as the ionization parameter (U) and the gas density (n_{H}).

Due to the complexity to model the Fe II ion, a valid approach is to consider the O I and Ca II ions as proxies of the former, under the assumption that they all form in clouds that are co-spatial. To analyze the role of the excitation mechanisms of O I and the physical conditions of the region emitting this line, [Matsuoka et al. \(2007\)](#) published simulations to probe the density and ionization parameter of this region. A similar approach was followed by [Matsuoka et al. \(2008\)](#) and more recently by [Martínez-Aldama et al. \(2015\)](#). Their results are based on the emission line flux ratios O I λ 11287/ λ 8446 and the ratio between the Calcium triplet and O I λ 8446. The first one is related to the role of the Ly β fluorescence in the O I emission while the second one traces the role of collisional excitation. Their results show that the O I, Ca II and Fe II lines arise in a region best characterized with $\log(n_{\text{H}})=11.5 \text{ cm}^{-3}$ and $\log(U)=-2.5$. These values are similar to those found in weak to moderate Fe II emitters.

The first interesting fact about O I λ 8446 and the Ca II triplet is that the relative intensities of these lines in PHL 1092 are different from what is usually observed in the literature. While O I λ 8446 is usually stronger than the Ca II triplet ([Riffel et al. 2006](#); [Landt et al. 2008](#)), PHL 1092 shows much stronger Ca II multiplets. For instance, [Matsuoka et al. \(2008\)](#) analyzing a sample of 11 quasars found a range of line ratios $0.2 < \text{O I } \lambda 11287/\lambda 8446 < 0.8$ and $0.3 < \text{Ca II}/\text{O I} < 0.8$. PHL 1092 has similar O I line ratios, $\text{O I } \lambda 11287/\lambda 8446=0.6$, but much higher Calcium triplet to O I λ 8446 flux ratio,

$\text{Ca II}/\text{O I}=3.0$. Indeed, each Ca II line from the triplet has individual fluxes roughly equal to that of O I.

Figure 7 from [Matsuoka et al. \(2007\)](#) shows isocontour curves in the U, n_{H} plane using the above line ratios. Based on the O I line ratio measured in PHL 1092, the ionization parameter and density are limited to $-2.4 < \log U < -4$ and $11.5 < \log n_{\text{H}} < 14 \text{ cm}^{-3}$, respectively. In addition, the Calcium to Oxygen line ratio measured for PHL 1092 implies $-2.0 < U < -4$ and $11.7 < n_{\text{H}} < 14 \text{ cm}^{-3}$. These values can be further constrained using the models presented by [Matsuoka et al. \(2008\)](#). The line ratios found from PHL 1092 place it in the parameter space consistent to $\log(U, n_{\text{H}})=(-3.0, 12.5 \text{ cm}^{-3})$.

[Negrete et al. \(2012\)](#) followed a different approach by considering UV line ratios. The set of diagrams presented by them involves flux ratios between emission lines of high- and mid-ionization potential such as Al III/Si III], Si IV/Si III, C IV/Al III, C IV/Si III], and Si IV/C IV.

Using Figure 5 of [Negrete et al. \(2012\)](#) and the observed UV line flux ratios in PHL 1092 listed in Table 2, we constrain the physical conditions in the BLR for every ratio employed. In order to achieve convergence, we also followed the approach of [Negrete et al. \(2012\)](#) (see their Figure 6). Given the error in the measurements, we found a convergence point at $\log(U, n_{\text{H}})=(-3.5, 13.0 \text{ cm}^{-3})$. These values are slightly different from those obtained for I Zw 1, $\log(U, n_{\text{H}})=(-2.0, 12.6 \text{ cm}^{-3})$ by [García-Rissmann et al. \(2012\)](#) and [Negrete et al. \(2012\)](#). Note however that PHL 1092 spectrum differs significantly from that of I Zw 1 (and other AGN with strong or weaker Fe II emission).

Are the above conditions derived from the UV lines consistent to those where the Fe II lines are formed in PHL 1092? In order to answer this question, we employed the predicted Fe II ratios listed in Table 2 of [García-Rissmann et al. \(2012\)](#), based on [Sigut & Pradhan \(2003\)](#) models. We found that for $\log(U, n_{\text{H}})=(-3.0, 12.6 \text{ cm}^{-3})$, the predicted Fe II line ratio $10502+11127/9200 \text{ \AA}$ is 0.35. In PHL 1092 it amounts to

0.45, in very good agreement with the models. Other combinations of values of U and n_H predict values in that ratio that that departs considerably from the observations.

From the results above we see that a combination of low ionization parameter and high gas density are necessary within the BLR to produce the observed emission lines. These results are consistent with the parameters derived by [Martínez-Aldama et al. \(2018a\)](#) for a sample of extreme population of quasars at high redshift. Their results show that weak C IV and C III] emission, strong Al III and a Si IV/C IV line flux ratio ~ 1 are common properties among quasars of extreme population A, to which PHL 1092 belongs. The similar physical properties derived for PHL 1092, which is a local source, with those found in objects at high redshift, suggest that the line ratio diagrams presented by [Negrete et al. \(2012\)](#) can be used as a selection method to search for extreme Fe II emitters candidates both in the local universe and at higher redshifts (up to $z \sim 3$).

With the launching of the *James Webb Space Telescope* in the next few years, this method can be used as a proxy to identify strong/extreme Fe II sources at a large stretch of cosmic age. There has been a lot of attention concerning the sources with $R_{4570} > 1.0$, as these sources (extreme Population A, or xA) seem to radiate at or toward a limiting Eddington ratio. This property can be exploited, under several assumptions for the use of these sources as cosmological probes ([Wang et al. 2013](#); [Marziani & Sulentic 2014](#)).

4.4 Excitation Mechanisms

Models employed to study the micro-physics of the Fe II transitions in AGN incorporate three main excitation mechanisms: collisional excitation, continuum fluorescence via UV resonance lines, and self fluorescence via overlapping Fe II transitions (see [Pradhan & Nahar 2011](#), for a comprehensive formulation of the problem). [Sigut & Pradhan \(1998\)](#) demonstrated that Lyman- α ($\text{Ly}\alpha$) fluorescence has an important role in the production of the optical Fe II lines. Their results show a significant increase in the strength of the 4570 Å bump when $\text{Ly}\alpha$ fluorescent is fully considered, in comparison when it is weakly (10%) or not included in the calculations.

The key aspect to confirm the fluorescent route for the Fe II emission is the presence of a bump of emission centered in $\lambda 9200$ and the detection of the $1 \mu\text{m}$ Fe II lines ([Rudy et al. 2000](#); [Rodríguez-Ardila et al. 2002](#); [Marinello et al. 2016](#)). The role of the different excitation mechanisms and physical conditions necessary to produce the Fe II emission can be investigated by analyzing the observed emission in different regions of the spectrum. NIR probes $\text{Ly}\alpha$ fluorescence and collisional excitation to energy levels of up to ~ 15 eV. Optical spectroscopy probes odd parity transitions of Fe II up ~ 5 eV while UV transitions, in addition, carries information about the density and ionization parameter.

In order to study the Fe II excitation mechanisms we follow the approach of [Marinello et al. \(2016\)](#), which consists of using line flux ratios between Fe II lines and the closest H I lines in the same spectrum. The observable quantities are: (i) $R_{4570} = F(\text{Fe II } 4570)/F(\text{H}\beta)$; (ii) the flux ratio of the Fe II bump centered at 9200 Å and the broad component of $\text{Pa}\gamma$, $R_{9200} = F(\text{Fe II } 9200)/F(\text{Pa}\gamma)$; and (iii) the flux ratio of the Fe II $1 \mu\text{m}$ lines ($\lambda 9998, \lambda 10502, \lambda 10890, \lambda 11127$) and

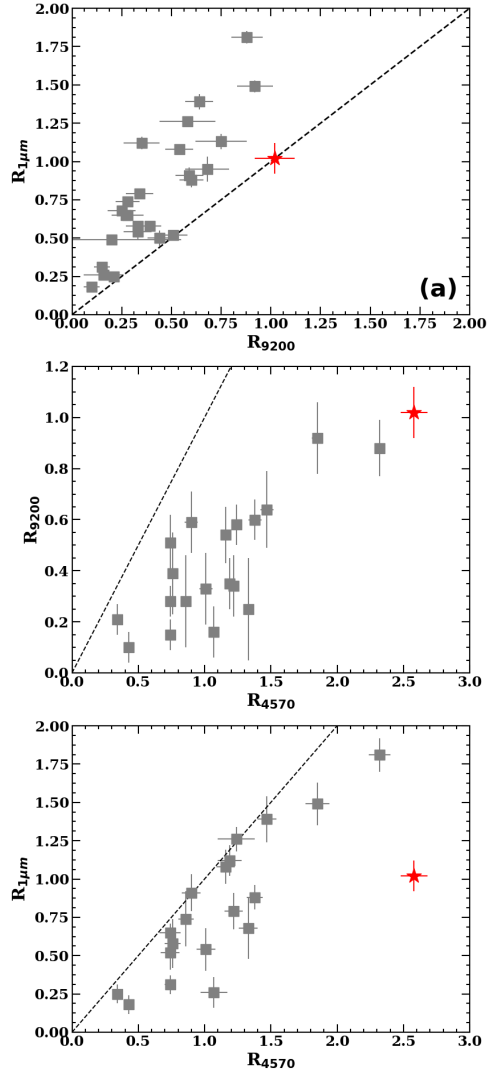


Figure 7. Fe II line ratios with respect to H β and Pa β in the optical and NIR, respectively. Panel (a) shows the correlation between the two groups of NIR Fe II lines important to this work, R_{9200} and $R_{1\mu\text{m}}$. Panel (b) shows the correlation between R_{9200} and the optical Fe II emission, R_{4570} . Panel (c) shows the correlation $R_{1\mu\text{m}}$ versus R_{4570} . In all panels, the grey squares represent the data from [Marinello et al. \(2016\)](#), the red star denotes PHL 1092, and the dashed black line is the equality line.

the broad component of Pa γ , $R_{1\mu\text{m}} = F(\text{Fe II } 1\mu\text{m})/F(\text{Pa}\gamma)$. Figure 7, shows the diagrams involving these quantities for PHL 1092 and other AGN from the literature.

The optical Fe II emission arises from photons emitted via levels $z^4(D,F) \rightarrow b^4F^e$. Figure 8 shows a partial Grotrian diagram for the most prominent transitions of Fe II ([Sigut & Pradhan 2003](#); [Pradhan & Nahar 2011](#)). In the diagram, red lines represent transitions leading to the bump at 9200 Å, violet lines show transitions responsible for the emission lines around 2800 Å and 1860 Å while blue lines show the transitions that form the bump centered at 4570 Å. Table 3 summarizes the main transitions that produce the NIR to UV Fe II emission. Note that other transitions are still present but they are weaker by a factor of 10 or more and for this reason they are not shown.

Table 3. Fe II transitions responsible for the bump centered at 4570Å.

Wavelength	Transitions	E_u (eV)	E_l (eV)
NIR Transitions			
11125.573	$b^4G_{5/2}^e \rightarrow z^4F_{3/2}^o$	6.727	5.613
10862.646	$b^4G_{7/2}^e \rightarrow z^4F_{5/2}^o$	6.727	5.587
10501.521	$b^4G_{9/2}^e \rightarrow z^4F_{7/2}^o$	6.726	5.546
9997.556	$b^4G_{11/2}^e \rightarrow z^4F_{9/2}^o$	6.721	5.482
9377.042	$u^4P_{1/2}^o \rightarrow d^4D_{3/2}^e$	11.263	9.937
9325.115	$u^4P_{3/2}^o \rightarrow d^4D_{5/2}^e$	11.270	9.937
9296.851	$u^4D_{5/2}^o \rightarrow d^4D_{5/2}^e$	11.238	9.900
9210.938	$u^4D_{1/2}^o \rightarrow d^4D_{1/2}^e$	11.307	9.957
9203.122	$v^4F_{3/2}^o \rightarrow d^4D_{1/2}^e$	11.308	9.957
9196.897	$u^4D_{3/2}^o \rightarrow d^4D_{3/2}^e$	11.288	9.937
9178.008	$v^4F_{5/2}^o \rightarrow d^4D_{3/2}^e$	11.291	9.937
9175.869	$v^4F_{7/2}^o \rightarrow d^4D_{5/2}^e$	11.255	9.900
9132.362	$v^4F_{9/2}^o \rightarrow d^4D_{7/2}^e$	11.206	9.845
9122.942	$u^4D_{7/2}^o \rightarrow d^4D_{7/2}^e$	11.208	9.845
9077.400	$u^4P_{3/2}^o \rightarrow d^4D_{5/2}^e$	11.270	9.900
9075.501	$v^4F_{5/2}^o \rightarrow d^4D_{5/2}^e$	11.270	9.900
8926.638	$u^4D_{5/2}^o \rightarrow d^4D_{7/2}^e$	11.238	9.845
Optical Transitions			
4629.337	$z^4F_{9/2}^o \rightarrow b^4F_{9/2}^e$	5.482	2.805
4583.822	$z^4D_{7/2}^o \rightarrow b^4F_{9/2}^e$	5.508	2.805
4582.831	$z^4F_{7/2}^o \rightarrow b^4F_{5/2}^e$	5.546	2.843
4576.339	$z^4D_{5/2}^o \rightarrow b^4F_{5/2}^e$	5.550	2.843
4555.878	$z^4F_{7/2}^o \rightarrow b^4F_{7/2}^e$	5.546	2.827
4549.462	$z^4D_{5/2}^o \rightarrow b^4F_{7/2}^e$	5.550	2.827
4541.524	$z^4D_{3/2}^o \rightarrow b^4F_{3/2}^e$	5.582	2.854
4522.632	$z^4D_{3/2}^o \rightarrow b^4F_{5/2}^e$	5.582	2.843
4520.207	$z^4F_{7/2}^o \rightarrow b^4F_{9/2}^e$	5.546	2.805
4515.345	$z^4F_{5/2}^o \rightarrow b^4F_{5/2}^e$	5.587	2.843
4508.284	$z^4D_{1/2}^o \rightarrow b^4F_{3/2}^e$	5.603	2.854
4491.414	$z^4F_{3/2}^o \rightarrow b^4F_{3/2}^e$	5.613	2.854
4489.179	$z^4F_{5/2}^o \rightarrow b^4F_{7/2}^e$	5.587	2.827
UV Transitions			
2884.764	$d^4D_{7/2}^e \rightarrow z^4D_{5/2}^o$	9.845	5.550
2882.190	$d^4D_{7/2}^e \rightarrow z^4F_{7/2}^o$	9.845	5.546
2872.258	$d^4D_{5/2}^e \rightarrow z^4F_{5/2}^o$	9.900	5.587
2869.317	$d^4D_{5/2}^e \rightarrow z^4D_{3/2}^o$	9.900	5.582
2858.629	$d^4D_{3/2}^e \rightarrow z^4D_{1/2}^o$	9.937	5.603
2856.908	$d^4D_{7/2}^e \rightarrow z^4D_{7/2}^o$	9.845	5.508
2856.454	$d^4D_{3/2}^e \rightarrow z^4F_{3/2}^o$	9.937	5.613
2851.721	$d^4D_{1/2}^e \rightarrow z^4F_{3/2}^o$	9.957	5.613
2848.315	$d^4D_{3/2}^e \rightarrow z^4F_{5/2}^o$	9.937	5.587
2848.110	$d^4D_{5/2}^e \rightarrow z^4D_{5/2}^o$	9.900	5.550
2845.601	$d^4D_{5/2}^e \rightarrow z^4F_{7/2}^o$	9.900	5.546
2839.507	$d^4D_{9/2}^e \rightarrow z^4F_{9/2}^o$	9.845	5.482
2831.881	$d^4D_{1/2}^e \rightarrow z^4D_{3/2}^o$	9.957	5.582
2824.566	$d^4D_{3/2}^e \rightarrow z^4D_{5/2}^o$	9.937	5.550
2820.954	$d^4D_{5/2}^e \rightarrow z^4D_{7/2}^o$	9.900	5.508
1877.716	$u^4G_{7/2}^o \rightarrow b^4G_{9/2}^e$	13.348	6.726
1872.973	$u^4G_{9/2}^o \rightarrow b^4G_{7/2}^e$	13.350	6.727
1872.638	$u^4G_{9/2}^o \rightarrow b^4G_{9/2}^e$	13.350	6.726
1869.553	$u^4G_{11/2}^o \rightarrow b^4G_{11/2}^e$	13.356	6.721
1843.260	$t^4G_{11/2}^o \rightarrow b^4G_{11/2}^e$	13.450	6.721
1841.710	$t^4G_{9/2}^o \rightarrow b^4G_{9/2}^e$	13.461	6.726
1839.999	$t^4G_{7/2}^o \rightarrow b^4G_{7/2}^e$	13.468	6.727
1839.802	$t^4G_{5/2}^o \rightarrow b^4G_{5/2}^e$	13.468	6.727

The 9200Å bump is a blend of lines produced by primary cascading from the energy levels around 13 eV, excited by the capture of a Ly α photon by an Fe II ion, via $u^4(P,D) \rightarrow e^4D$ and $v^4F \rightarrow e^4D$. Secondary cascading occurs from the levels e^4D , at about 10 eV, to the upper levels from which the optical emission lines are produced, after the emission of UV photons at $\sim 2800\text{\AA}$, via $e^4D \rightarrow z^4(D,F)$. Since the energy to excite the $u^4(P,D)$ and v^4F levels are too high to be excited by mechanisms other than Ly α fluorescence, the detection of the 9200Å bump probes unambiguously the presence of that mechanism.

Figure 7(a) shows R_{9200} versus $R_{1\mu m}$. The grey dots from Marinello et al. (2016) suggest a correlation between these two ratios. The inclusion of PHL 1092 in the plot introduces some scatter to the high end of the correlation. The $1\mu m$ lines result from secondary cascading of the Ly α fluorescence process, e.g., after a Fe II ion captures a Ly α photon, electrons are excited to levels at $\sim 15\text{eV}$, $(t,u)^4G$, which cascade down via $(t,u)^4G \rightarrow b^4G$ emitting photons at around 1860Å. In the secondary cascading, the $1\mu m$ lines are emitted via $b^4G \rightarrow z^4(D,F)$, populating the energy levels from which the bulk of the optical Fe II is produced. Note that the b^4G level needs only ~ 6 eV to be excited, thereby collisional excitation is also a possible mechanism to pump this level. The strong correlation observed in Figure 7(a) shows the importance of the Ly α fluorescence in the production of the $1\mu m$ Fe II lines.

Garcia-Rissmann et al. (2012) used a grid of Fe II models in the NIR in order to create an Fe II template. They found that models with $\log(U, n_H) = (-2.0, 12.6 \text{ cm}^{-3})$ best reproduce the Fe II emission in IZw 1. In their models, the strength of the $1\mu m$ lines is reduced relative to that of the 9200Å bump for models with the parameters we derived in this work, e.g., $\log(U, n_H) = (-3.0, 13.0 \text{ cm}^{-3})$. This reduction is indeed observed in PHL 1092, producing its departure from the main trend observed in the Figure 7(a).

Figure 7(b) shows R_{4570} versus R_{9200} . This plot strengthens the importance of the Ly α fluorescence in the production of the optical Fe II emission. Since the 9200Å bump is produced exclusively by that mechanism, the plot gives us a rough estimate of the percentage of its contribution to the optical emission.

Marinello et al. (2016) found a strong correlation between the above two ratios. However, their sample did not include extreme strong Fe II emitters ($R_{4570} > 2.5$). We see that the correlation still holds after the inclusion of PHL 1092 in the diagram. The physical conditions derived in the previous section, $\log(U, n_H) = (-3.0, 13.0 \text{ cm}^{-3})$, enhance the Ly α fluorescence. Very likely, the R_{9200} measured in PHL 1092 is expected to be close to the maximum possible for the given Pa β flux. In PHL 1092 the contribution of Ly α fluorescence to the Fe II emission is not only important, as in AGN with weak Fe II, but also crucial to enhance the Fe II bump at 4570Å. Since the 4570Å bump can be pumped by other excitation mechanisms (i.e. collisional excitation) we would expect, in theory, that it keeps increasing while R_{9200} should remain roughly constant, with values around one, at the high end of the correlation. Note that the three strong Fe II emitters ($R_{4570} > 2.0$) displayed in the plot have similar R_{9200} as R_{4570} grows. If we assume that the optimal physical conditions for Ly α fluorescence is met, a maximum value for the R_{9200} should be reached while the R_{4570}

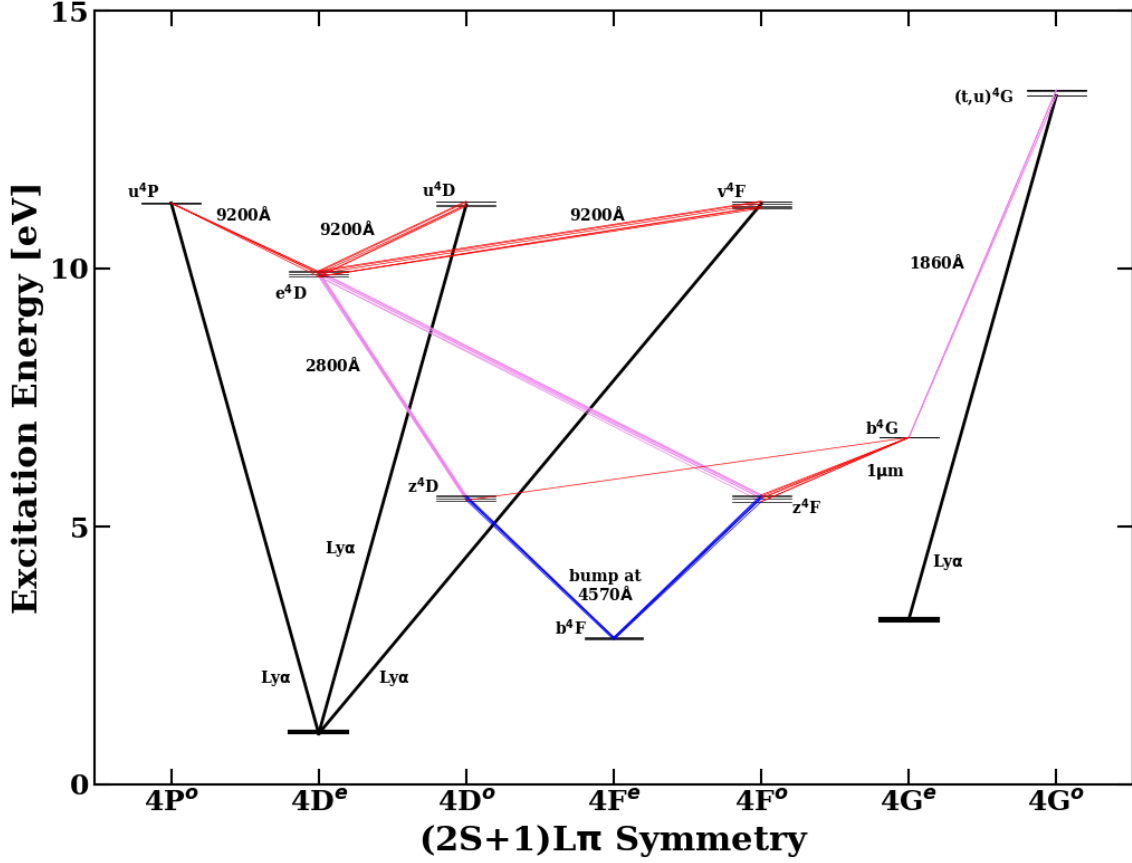


Figure 8. Partial Grotrian diagram for the Fe II emission. The diagram shows the main transition that from primary and/or secondary cascading after a Ly α photon is absorbed that populate the $z^4(D,F)$ levels, from which the optical Fe II bump (centered at 4570Å) is emitted via $z^4(D,F) \rightarrow b^4F^e$ (blue line). Red lines show the NIR primary and secondary cascade transitions after a Fe II ion absorbs a Ly α photon, e.g. the bump at 9200Å and the 1 μ m lines. Violet lines represent the UV transitions that populated directly or indirectly the $z^4(D,F)$ levels.

keeps growing towards $R_{4570} \sim 3$. This behaviour is expected from the perspective of photon balance and the intrinsic cascading process of Ly α fluorescence, because every photon from the 9200Å blend produces a photon in the 4570Å bump under the assumption of zero extinction. Note that a photon emitted by the 9200Å bump has an energy equals to $E_{9200} = 2.16 \times 10^{-12}$ erg while a photon from 4570Å has $E_{4570} = 4.35 \times 10^{-12}$ erg, roughly the double of the energy. This means that it is necessary twice as much energy to increase R_{4570} compared with that of R_{9200} . Therefore, a flattening in the high end of the correlation is expected.

Figure 7(c) shows R_{4570} versus $R_{1\mu m}$. The importance of this plot is on the fact that the levels $z^4(D,F)$, from which the optical Fe II emission is produced, are populated after the 1 μ m lines are emitted via $b^4G \rightarrow z^4(D,F)$. The energy necessary to excite b^4G is ~ 6 eV and can be reached by two main excitation mechanisms: collisional excitation and Ly α fluorescence (Marinello et al. 2016).

Figure 7(a) confirms the trend between R_{9200} and $R_{1\mu m}$,

with some scatter for strong Fe II emitters, suggesting Ly α fluorescence as an important mechanism for the 1 μ m lines. Moreover, for PHL 1092 the values of R_{9200} and $R_{1\mu m}$ are similar, which suggests that Ly α fluorescence must have an even more importance in the formation of these lines. If we assume that both transitions have similar probability, then the contribution of the Ly α fluorescence in the production of the 1 μ m lines should also be optimal for these lines for the physical conditions within the BLR. Note that as in Figure 7(b) we cannot expect the correlation to grow to extreme values of $R_{1\mu m}$. The discussion above made for Figure 7(b) can also be applied for this case since the 1 μ m photons have similar energy ($E_{1\mu m} = 1.99 \times 10^{-12}$ erg) that the ones from the 9200Å bump.

The results gathered from Figure 7 suggest that the main excitation mechanism pumping the Fe II emission in PHL 1092 is Ly α fluorescence. In contrast, weaker Fe II emitters have their emission driven by collisional excitation, as found by Marinello et al. (2016). Note that other parameters

may also contribute in the enhancement of the Fe II emission in AGN. For instance, [Sigut & Pradhan \(2003\)](#) showed that the presence of micro-turbulence (η_t) in the BLR clouds can also increase the efficiency of the Fe II production (their models uses $\eta_t = 10 \text{ km s}^{-1}$). [Garcia-Rissmann et al. \(2012\)](#) showed that for that η_t and $\log(U, n_H) = (-2.0, 12.6 \text{ cm}^{-3})$ the [Sigut & Pradhan \(2003\)](#) models reproduce well the Fe II emission even in IZw 1, a strong Fe II emitter. [Bruhweiler & Verner \(2008\)](#) found that doubling the turbulence, $\eta_t = 20 \text{ km s}^{-1}$, in combination with a larger ionization parameter and a slighter lower density, the predicted Fe II emission also reproduces well the observed IZw 1 spectrum in optical/UV regions. Thus, increasing the turbulence velocity increases also the probability of a Ly α photon to be captured by an Fe II ion, thereby increasing the relevance of the Ly α fluorescence in the observed Fe II emission. This could be the case for PHL 1092. That is, in that source we are probing a higher turbulence velocity for the gas in the BLR.

Another alternative for the pumping of the Fe II emission in extreme Fe II emitters is a higher chemical abundance in the BLR. Based on simulations, [Panda et al. \(2018\)](#) showed that increasing the BLR metallicity leads to a significant increase in R_{4570} . They showed that a $Z = 3 Z_\odot$ produces nearly twice the Fe II emission than at solar metallicity. Indeed, an increase of R_{4570} by a factor of 3 can be obtained when $Z = 10 Z_\odot$.

[Negrete et al. \(2012\)](#) analyzed the physical condition of the BLR in two strong Fe II emitters, IZw 1 and SDSS J12014+0116. They found that an abundance five times solar in Aluminum and Silicon was associated to a higher ionization parameter and a lower density, $\log(U, n_H) = (-2.75, 12.3 \text{ cm}^{-3})$. These values, consistent with [Garcia-Rissmann et al. \(2012\)](#) and [Sigut & Pradhan \(2003\)](#) models, would reproduced the observed UV line ratios in the spectra. One possible route to increase the metallicity in the BLR would be through supernova activity in the circumnuclear region, whose ejecta could enrich the AGN surrounding media. The over-solar matter then would be transported towards the BLR via inflows.

Observations give support to this scenario. [Watabe et al. \(2008\)](#) had already found that the nuclear starburst luminosity in nearby AGN was dependent on the AGN Eddington ratio while [Hennig et al. \(2018\)](#) found in the local NLS1 galaxy, Mrk 42, a starburst nuclear ring. Another possibility is that the strong outflows detected in C IV and Si IV by means of blueshifted components, swept away heavy elements, thereby increasing the metallicity. Atoms such as Carbon and Silicon, are efficiently accelerated by resonance line scattering (i.e., in a “line driven wind” scenario). Therefore, the outflowing gas may appear enriched with respect to the accretion disk gas ([Baskin & Laor 2012](#)). Since the models of [Sigut & Pradhan \(2003\)](#) and the template of [Garcia-Rissmann et al. \(2012\)](#) were constructed for Solar abundances, the higher abundance scenario cannot be currently tested. However, the models presented in [Garcia-Rissmann et al. \(2012\)](#) show a clear increase in the 9200Å bump for the physical parameters obtained in this work and are also consistent with the line ratios in the observed spectrum of PHL 1092. These results support that a lower ionization parameter and a higher density are the most likely cause of the increase efficiency of the Ly α fluorescence in PHL 1092. Simulations with a more focused grid of parameters, high spa-

tial resolution observations, and a bigger sample of extreme Fe II emitters are necessary to draw more robust conclusions about these hypothesis.

5 CONCLUSIONS

In this work we present a panchromatic (UV, optical and NIR) analysis of the extreme strong Fe II emitter PHL 1092. We combine optical and NIR spectroscopic observations to estimate several physical properties of this outstanding source. Using template modeling of the Fe II spectrum, we were able to estimate accurately the intensity of that emission. Emission lines were fitted using a Lorentzian model in order to obtain their fluxes and line widths. The main results obtained from these measurements are summarized below:

- We re-estimated the R_{4570} ratio in PHL 1092 using a more robust approach. Our results show a $R_{4570} = 2.58$, significantly smaller than the values reported previously, of up to $R_{4570} = 6.2$. This new value, however, still places PHL 1092 among the strongest Fe II emitters ever observed.

- The FWHM obtained for Fe II, O I, and Ca II suggest that the clouds emitting these ions are co-spatial, since they share roughly the same line width and shape. Compared with H β , the FWHM of these lines are significantly smaller, suggesting that the clouds emitting low ionization ions are in the outer portion of the BLR while H β is emitted in the mid-portion of that region.

- Emission line flux ratios in the and UV in PHL 1092 suggest high densities ($n_H \sim 10^{13.0} \text{ cm}^{-3}$) and a low ionization parameter ($\log U \sim -3.5$) for the Fe II emitting gas. This result is consistent with the parameters employed to create the NIR Fe II template in [Garcia-Rissmann et al. \(2012\)](#).

- We found an excess of Fe II emission in the 9200Å bump. Since this emission can only be produced by Ly α fluorescence, we suggest that this excitation mechanism is pumping up the bulk of the Fe II emission in PHL 1092. This result contrasts to what is found in weaker Fe II emitters, where collisional excitation seems to be the main driver of that emission.

- The re-estimated value of R_{4570} places PHL 1092 among the extreme quasars in the main quasar sequence defined by the optical plane of the Eigenvector 1. In this plane, PHL 1092 is classified as **extreme** ‘Population A’ AGN due its high R_{4570} and low $\text{FWHM}_{\text{H}\beta}$.

Our work points out towards intrinsic differences in the physical conditions of the BLR in this extreme Fe II emitter even though the gas distribution follows the same trend as in normal Fe II emitters. A follow-up investigation of this issue using a larger sample of ‘PHL 1092-like’ sources is necessary to fully support our conclusions on the physical conditions driving the Fe II emission along the E1 plane.

ACKNOWLEDGEMENTS

A.R.-A. acknowledges partial support from CNPq Fellowship (311935/2015-0 & 203746/2017-1). M.M. acknowledges partial support from PCI Fellowship PM acknowledges funding from the INAF PRIN-SKA 2017 program 1.05.01.88.04.

REFERENCES

- Barth, A. J., Pancoast, A., Bennert, V. N., et al. 2013, *ApJ*, 769, 128
- Baskin, A. & Laor, A. *MNRAS*, 426, 1144
- Bergeron & Kunth, 1980, *A&A*, 85L, 11B
- Bian W., Yuan Q., Zhao Y., 2005, *MNRAS*, 364, 187B
- Boroson T. A. & Green R. F., 1992, *ApJS*, 80, 109B
- Boroson T., 2002, *ApJ*, 565, 78B
- Boroson T., 2005, *AJ*, 130, 381B
- Brotherton, M. S.; Tran, Hien D.; Becker, R. H.; Gregg, Michael D.; Laurent-Muehleisen, S. A.; White, R. L., 2001, *ApJ*, 546, 775
- Bruhweiler F., Verner E., 2008, *ApJ*, 675, 83B
- Clemens et al., 2004 *ApJ*, 576L, 9Z
- Cracco, V.; Ciroi, S.; Berton, M.; Di Mille, F.; Foschini, L.; La Mura, G.; Rafanelli, P., 2016, *MNRAS*, 462, 1256C
- Czerny, B.; Nikolajuk, M.; Piasecki, M.; Kuraszekiewicz, J., 2001, *MNRAS*, 325, 865C
- Coatman, Liam; Hewett, Paul C.; Banerji, Manda; Richards, Gordon T., 2016, *MNRAS*, 461, 647C
- Dasgupta, S.; Rao, A. R.; Dewangan, G. C. 2004, *ApJ*, 614, 626D
- Dong, Xiao-Bo; Ho, Luis C.; Wang, Jian-Guo; Wang, Ting-Gui; Wang, Huiyuan; Fan, Xiaohui; Zhou, Hongyan, 2010, *ApJ*, 721, 143D
- Du, P., Lu, K.-X., Hu, C., et al. 2016, *ApJ*, 820, 27
- Du, P., Zhang, Z.-X., Wang, K., et al. 2018, *ApJ*, 856, 6
- Dultzin-Hacyan, D.; Taniguchi, Y.; Uranga, L. 1999, *ASPC*, 175, 303
- Elias, Jonathan H.; Joyce, Richard R.; Liang, Ming; Muller, Gary P.; Hileman, Edward A.; George, James R., 2006, *Proceedings of SPIE*, 6269E, 4CE
- Ferland, Gary; van Hoof, Peter; Verner, Dima; Verner, Katya; Ferguson, Jason; Hamann, Fred; Kingdon, Jim; Korista, Kirk; Shields, Jo, 1999, *Astrophysics Source Code Library*, 9910.001
- García-Rissmann, A., Rodríguez-Ardila, A., Sigut, T. A. A. & Pradhan, A. K., 2012, *ApJ*, 751, 7
- Glikman, Eilat; Helfand, David J.; White, Richard L., 2006, *ApJ*, 640, 579
- Goodrich R. W., 1989, *ApJ*, 342, 224G
- Granato & Danese, 1994 *ApJ*, 576L, 9Z
- Hennig, Moiré G.; Riffel, Rogemar A.; Dors, O. L.; Riffel, Rogerio; Storchi-Bergmann, Thaisa; Colina, Luis, 2018, *MNRAS*, 477, 1086H
- Hu C., Wang J.-M., Ho L. C., Chen Y.-M., Zhang H.-T., Bian W.-W., Xue S.-J., 2008, *ApJ*, 687, 78H
- Hu, Chen; Du, Pu; Lu, Kai-Xing; Li, Yan-Rong; Wang, Fang; Qiu, Jie; Bai, Jin-Ming; Kaspi, Shai; Ho, Luis C.; Netzer, Hagai; Wang, Jian-Min; SEAMBH Collaboration, 2015, *ApJ*, 834, 138
- Joly M., 1991, *A&A*, 242, 49j
- Joly M., 1993, *Ann. Phys.(Paris)*, 18, 241J
- Kollatschny, W., Zetzl, M., & Dietrich, M. 2006, *A&A*, 454, 459
- Komossa S., Voges W., Xu D., Mathur S., Adorf H.-M., Lemson G., Duschl W. J. Grupe D., 2006, 132, 531K
- Kovačević J., Popović L. Č., Dimitrijević M. S., 2010, *ApJS*, 189, 15K
- Landt, H, Bentz, M. C., Ward, M. J., Elvis, M, Peterson, B. M., Korista, K. T. & Karovska, M. 2012, *ApJS*, 174, 282
- Lawrence, A.; Saunders, W.; Rowan-Robinson, M.; Crawford, J.; Ellis, R. S.; Frenk, C. S.; Efstathiou, G.; Kaiser, N., 2012, *MNRAS*, 235, 261L
- Lawrence, A.; Elvis, M.; Wilkes, B. J.; McHardy, I.; Brandt, N., 1997, *MNRAS*, 285, 879l
- Leighly K. M., 1999, *ApJS*, 125, 317L
- Leighly K. M. & Moore J. R., 2004, *ApJ*, 611, 107L
- Leighly, K. M.; Dietrich, M. & Barber, S., 2011, *ApJ*, 728, 94
- Lipari, Sebastian; Terlevich, Roberto; Macchetto, F., 1993, *ApJ*, 406, 451
- Marinello M., Rodríguez-Ardila R., García-Rissmann A., Sigut T. A. A., Pradhan A. K., 2016, *ApJ*, 820, 116M
- Martínez-Aldama, Mary Loli; Dultzin, Deborah; Marziani, Paola; Sulentic, Jack W.; Bressan, Alessandro; Chen, Yang; Stirpe, Giovanna M., 2015, *ApJS*, 217, 3M
- Martínez-Aldama, M. L.; del Olmo, A.; Marziani, P.; Sulentic, J. W.; Negrete, C. A.; Dultzin, D.; D’Onofrio, M.; Perea, J. 2018, *A&A*, 618, 179M
- Martínez-Aldama, M. L.; del Olmo, A.; Marziani, P.; Negrete, C. A.; Dultzin, D.; Martínez-Carbalho, M. A. 2018, <https://arxiv.org/pdf/1801.04570.pdf>
- Marziani, P., Sulentic, J. W., Stirpe, G. M., Zamfir, S., & Calvani, M. 2009, *MNRAS*, 495, 83
- Marziani, P., Sulentic, J. W., Zwitter, T., Dultzin-Hacyan, D., & Calvani, M. 2001, *ApJ*, 558, 553
- Marziani, P., Zamanov, R. K., Sulentic, J. W., & Calvani, M., 2003, *MNRAS*, 345, 1133
- Marziani, P.; & Sulentic, J. W. 2014, *MNRAS*, 442, 1211
- Marziani, P.; Dultzin, D.; Sulentic, J. W.; Del Olmo, A.; Negrete, C. A.; Martínez-Aldama, M. L.; D’Onofrio, M.; Bon, E.; Bon, N.; Stirpe, G. M., 2018, *FraAS*, 5, 6M
- Mason, R. E.; Rodríguez-Ardila, A.; Martins, L.; Riffel, R.; González Martín, O.; Ramos Almeida, C.; Ruschel Dutra, D.; Ho, L. C.; Thanjavur, K.; Flohic, H.; Alonso-Herrero, A.; Lira, P.; McDermid, R.; Riffel, R. A.; Schiavon, R. P.; Winge, C.; Hoenic, M. D.; Perlman, E., 2015, *ApJS*, 217, 13M
- Matsuoka Y., Oyabu S., Tsuzuki Y., Kawara K., 2007, *ApJ*, 663, 781M
- Matsuoka, Y.; Kawara, K.; Oyabu, S., 2008, *ApJ*, 673, 62
- Miniutti, G.; Fabian, A. C.; Brandt, W. N.; Gallo, L. C.; Boller, Th., 2009, *MNRAS*, 396L, 85M
- Miniutti, G.; Brandt, W. N.; Schneider, D. P.; Fabian, A. C.; Gallo, L. C.; Boller, Th., 2012, *MNRAS*, 425, 1718M
- Moran E. C. Halpern J. P., Helfand D. J., 1996, *ApJS*, 106, 341M
- Negrete, C. Alenka; Dultzin, Deborah; Marziani, Paola; Sulentic, Jack W. 2012, *ApJ*, 757, 62N
- Negrete, C. A.; Dultzin, D.; Marziani, P.; Esparza, D.; Sulentic, J. W.; del Olmo, A.; Martínez-Aldama, M. L.; García López, A.; D’Onofrio, M.; Bon, N.; 2018, *A&A*, 620, 118N
- Netzer, H.; & Trakhtenbrot, B., 2007, *ApJ*, 654, 754
- Netzer, H.; & Marziani, P. 2010, *ApJ*, 724, 318N
- Nikolajuk, M.; Czerny, B.; Gurynowicz, P. 2009, *MNRAS*, 394, 2141N
- Osterbrock D. E. & Pogge R. W., 1985, *ApJ*, 297, 166O
- Panda, S., Czerny, B., Adhikari, T. P., et al. 2018, *ApJ*, 866, 115
- Pecaut, M. J., & Mamajek, E. E., 2013, *ApJS*, 208, 9
- Peterson, B. M.; Ferrarese, L.; Gilbert, K. M.; Kaspi, S. et al., 2004, *ApJ*, 613, 682
- Pradhan, A. K. & Nahar, S. N., 2011, *Atomic Astrophysics and Spectroscopy* (Cambridge: Cambridge Univ. Press)
- Rafter, S. E., Kaspi, S., Chelouche, D., et al. 2013, *ApJ*, 773, 24
- Rakshit, S.; Stalin, C. S.; Chand, H.; Zhang, X.-G., C. S., 2017, *ApJS*, 229, 39R
- Riffel, R., Rodríguez-Ardila, A. & Pastoriza, M. G., 2006, *A&A*, 457, 61
- Rodríguez-Ardila R., Viegas, S. M.; Pastoriza, M. G.; Prato, L., 2002, *ApJ*, 565, 140L
- Rodríguez-Ardila, A & Mazzalay, X., 2006 *ApJ*, 576L, 9Z
- Rodríguez-Ardila, A. & Mazzalay, X., 2007, *MNRAS*, 376, 57
- Rudy, Richard J.; Mazuk, S.; Puetter, R. C.; Hamann, F. 2000, *ApJ*, 376, 57
- Ryan C. J., De Robertis M. M., Virani S., Laor A., Dawson P. C., 2007, *ApJ*, 539, 166R
- Sameshima, H.; Kawara, K.; Matsuoka, Y.; Oyabu, S.; Asami, N.; Ienaka, N., 2011, *mnras*, 410,1018S
- Skrutskie, M. F.; Cutri, R. M.; Stiening, R.; Weinberg, M. D.; Skrutskie, S.; Carpenter, J. M.; Beichman, C.; Capps, R.

- Chester, T.; Elias, J.; and 21 coauthors, 2006, *AJ*, 131, 1163
- Shen Y. et al., 2011, *ApJS*, 194, 45S
- Shen Y. & Ho L. C., 2014, *Nature*, 513, 210S
- Sigut T. A. A. & Pradhan A. K., 1998, *ApJ*, 499L, 139S
- Sigut T. A. A. & Pradhan A. K., 2003, *ApJS*, 145, 15S
- Shen et al., 2011 *ApJ*, 576L, 9Z
- M. Śniegowska , B. Czerny, B. You, S. Panda, J.-M. Wang, K. Hryniewicz, and C. Wildy, 2018, *ArXiv:1701.03694*
- Sulentic, J. W., Stirpe, G. M., Marziani, P., et al. 2004, *A&A*, 423, 121
- Sulentic, J. W.; Marziani, P., 1999, *ApJ*, 518, 1
- Sulentic, J. W., Marziani, P., and Dultzin-Hacyan, D., 2000a, *Ann. Rev. Astron. Astrophys.* 38, 521
- Sulentic, J. W., Marziani, P., Zwitter, T., Dultzin-Hacyan, D., and Calvani, M., 2000b, *ApJ*, 545, L15
- Sulentic J. W., Zwitter T., Marziani P., Dultzin-Hacyan D., 2000, *ApJ*, 536L, 5S
- Sulentic J. W., Marziani P., Zamanov R., Bachev R., Calvani M., Dultzin-Hacyan D., 2002, *ApJ*, 566L, 71S
- Sulentic, J. W.; Bachev, R.; Marziani, P.; Negrete, C. A.; Dultzin, D., 2007, *ApJ*, 666, 757S
- Tsuzuki, Y., Kawara, K., Yoshii, Y., Oyabu, S., TanabĀP, T. & Matsuoka, Y., 2006, *ApJ*, 650, 57
- Vanden Berk, Daniel E.; Richards, Gordon T.; Bauer, Amanda; Strauss, Michael A. et al, 2001, *AJ*, 122, 549
- Verner, E. M.; Verner, D. A.; Korista, K. T.; Ferguson, J. W.; Hamann, F.; Ferland, G. J., 1999, *ApJS*, 120, 101
- VĀron-Cetty, M.-P., Joly, M. & Vĕron, P., 2004, *A&A*, 417, 515
- Verner E. M., Verner D. A., Korista K. T., Ferguson J. W., Hamann F., Ferland G. J., 1999, *ApJS*, 120, 101V
- Vestergaard, M. & Wilkes, B. J., 2001, *ApJS*, 134, 1
- Wang, J.-M.; Du, P.; Valls-Gabaud, D.; Hu, C.; Netzer, H., 2013, *PhRvL*, 110, 081301
- Watabe, Y.; Kawakatu, N. & Imanishi, M., 2008, *ApJ*, 677, 895
- Wildy, C., Landt, H., Goad, M. R., Ward, M. & Collinson, J. S., 2016, *MNRAS*, 461, 2085
- Bruhweiler F., Verner E., 2008, *ApJ*, 675, 83B
- Wills, B. J., Shang Z. Yuan J. M., 2000, *NewAR*, 44,511W
- Zhou, Hongyan; Wang, Tinggui; Yuan, Weimin; Lu, Honglin; Dong, Xiaobo; Wang, Junxian; Lu, Youjun., 2006, *ApJS*, 166, 128Z
- Zamanov R., Marziani P., Sulentic J. W., Calvani M., Dultzin-Hacyan D., Bachev R., 2002, *ApJ*, 576L, 9Z

This paper has been typeset from a $\text{\TeX}/\text{\LaTeX}$ file prepared by the author.